

Accepted to the Astrophysical Journal, Jan. 23, 2017

Residual Gas & Dust Around Transition Objects and Weak T Tauri Stars¹Greg W. Doppmann², Joan R. Najita³, and John S. Carr⁴

gdoppmann@keck.hawaii.edu

najita@noao.edu

carr@nrl.navy.mil

ABSTRACT

Residual gas in disks around young stars can spin down stars, circularize the orbits of terrestrial planets, and whisk away the dusty debris that is expected to serve as a signpost of terrestrial planet formation. We have carried out a sensitive search for residual gas and dust in the terrestrial planet region surrounding young stars ranging in age from a few Myr to ~ 10 Myr in age. Using high resolution $4.7\mu\text{m}$ spectra of transition objects and weak T Tauri stars, we searched for weak continuum excesses and CO fundamental emission, after making a careful correction for the stellar contribution to the observed spectrum. We find that the CO emission from transition objects is weaker and located further from the star than CO emission from non-transition T Tauri stars with similar stellar accretion rates. The difference is possibly the result of chemical and/or dynamical effects (i.e., a low CO abundance or close-in low-mass planets). The weak T Tauri stars show no CO fundamental emission down to low flux levels ($5 \times 10^{-20} - 10^{-18} \text{ W m}^{-2}$). We illustrate how our results can be used to constrain the residual disk gas content in these systems and discuss their potential implications for star and planet formation.

Subject headings: infrared: stars – stars: formation, pre-main sequence — stars: circumstellar matter, protoplanetary disks — techniques: spectroscopic, radial velocities

²W.M. Keck Observatory, 65-1120 Mamalahoa Hwy, Kamuela HI 96743

³National Optical Astronomy Observatory, 950 N. Cherry Ave., Tucson, AZ 85719, USA

⁴Naval Research Laboratory, Code 7213, Washington, DC 20375, USA

¹Data presented herein were obtained at the W.M. Keck Observatory from telescope time allocated to the National Aeronautics and Space Administration through the agency's scientific partnership with the California Institute of Technology and the University of California. The Observatory was made possible by the generous financial support of the W.M. Keck Foundation.

1. Introduction

The circumstellar disks that surround stars at birth are believed to dissipate through a combination of processes that include accretion, planet formation, and photoevaporation (Alexander et al. 2014). In this way, stars evolve from accreting stars surrounded by an optically thick disk of gas and dust that extends in to the stellar surface (a typical classical T Tauri star; CTTS) to stars with little evidence for stellar accretion or a surrounding dust disk (a weak T Tauri star; WTTS). While most stars are CTTS at 1–2 Myr of age, almost all are WTTS beyond 5 Myr of age, based on the measured stellar accretion rates and dust continuum excesses associated with young stars (e.g., Mamajek 2009; Sicilia-Aguilar et al. 2006; Williams & Cieza 2011). The unusual spectral energy distributions (SEDs) of the population of young stars called transition objects (TOs), which have a significant continuum excess at long wavelengths ($> 10\mu\text{m}$) and a weak excess at short wavelengths ($< 10\mu\text{m}$), are thought to represent an intermediate, transitional, phase of evolution between CTTS and WTTS.

In charting out disk evolution, the dust component is readily probed by continuum excesses, through the use of SEDs when the excess is strong and through high resolution spectroscopy when the excess is weak (e.g., Hartigan et al. 1989, 1991; Valenti et al. 1993). It is important to probe directly the lifetime of the gaseous component, because the dust may not reliably trace the gas. A residual dust disk in the WTTS phase might be a signature of accompanying residual gas. Alternatively, it could be unrelated to the evolution of the gaseous disk, e.g., if it is post-accretion debris produced by terrestrial planet formation or collisions of planetesimals leftover from the planet formation process (Kenyon & Bromley 2004; Raymond et al. 2011, 2012), i.e., similar to the situation for HD 21997 (Kóspál et al. 2013) but at much smaller radii. A residual gas disk might also persist in the absence of dust.

The extent and lifetime of residual gas disks is important for our understanding of planet formation and stellar rotation. Residual gas disks at AU distances may affect the outcome of terrestrial planet formation by damping the eccentricities of forming terrestrial planets or proto-planets and/or inducing their radial migration (Kominami & Ida 2002; Agnor & Ward 2002). If residual gas persists long enough to damp terrestrial planet eccentricities, it would help to explain the low eccentricities of terrestrial planets in the solar system and surrounding other stars (Hadden & Lithwick 2014; Shabram et al. 2016; Van Eylen & Albrecht 2015).

Residual gas in the terrestrial planet region may help to reconcile the large discrepancy between the high occurrence rate of Earth-mass exoplanets ($\sim 20\%$) and the much lower incidence rate (few %) of the warm debris that is the expected signpost of terrestrial planet formation at ages of ~ 10 Myr. A residual gas disk with a column density $> 10^{-5}$ of the minimum mass solar nebula (MMSN) that persists during the epoch of terrestrial planet assembly can quickly remove small grains from the terrestrial planet region or prevent their formation (Kenyon et al. 2016). If either occurs, warm debris is not the reliable beacon of terrestrial planet formation that it is commonly regarded to be (Kenyon & Bromley 2004; Raymond et al. 2011, 2012; Leinhardt et al. 2015).

Residual gas within 0.5 AU that persists into the WTTS phase could also play a role in regulating the rotation rates of young stars (see Bouvier et al. 2014, for a review) through the coupling of stars to their gaseous inner disks via stellar magnetic fields (“disk locking”). Gallet & Bouvier (2013) have shown that the rotational periods of stars as a function of age can be explained if solar mass stars remain magnetically locked to their gaseous inner disks for 5 Myr on average.

Despite its potential significance for the outcome of star and planet formation, residual disk gas is more difficult to study than residual dust, especially with *in situ* gas diagnostics. As a result, stellar accretion rates are often used as a surrogate diagnostic. The decline in stellar accretion with time (e.g., Sicilia-Aguilar et al. 2006, 2010) is consistent with the picture of a dissipating gaseous disk. Surveys of both NIR excesses and stellar accretion find that fewer than 15% of young stars show evidence of an inner disk at 5 Myr (e.g., Briceno et al. 2005; Hernandez et al. 2005; Fedele et al. 2010). Stellar accretion rates would be a good probe of residual gas if we could be certain that all of the gas in the disk is actively accreting. However, the reliability of this assumption is an open question. It is therefore of interest to know whether gaseous inner disks survive for much longer than either the inner dust disk or gaseous accretion onto the star.

Here we explore this issue by carrying out a sensitive search for *in situ* emission from residual gas in disk systems with low stellar accretion rates. We use high resolution $4.7\mu\text{m}$ spectroscopy to search for CO ro-vibrational emission which probes residual gas in the terrestrial planet region of the disk. Thermally excited CO requires high density ($> 10^{10} \text{ cm}^{-3}$) and temperature ($> 500 \text{ K}$) to emit, conditions that are characteristic of the inner disks of T Tauri stars. Detected from almost all CTTS, CO ro-vibrational emission probes disk radii from the inner disk edge to $\sim 1 \text{ AU}$ for typical CTTS, based on spectroscopically resolved CO emission. These properties make it an attractive probe of gaseous disks in the terrestrial planet region (Najita et al. 2003, 2007; Brittain et al. 2003, 2007; Blake & Boogert 2004; Rettig et al. 2004; Salyk et al. 2008, 2009, 2011; Brown et al. 2013; Banzatti & Pontoppidan 2015).

CO emission from transition objects has been studied previously (Najita et al. 2003, 2008; Rettig et al. 2004; Salyk et al. 2007, 2009; Pontoppidan et al. 2008), although similar studies have not been carried out for WTTS. Because the strength of the emission tends to decline with decreasing accretion rate (Najita et al. 2003; Brittain et al. 2007), it is important in studying WTTS to optimize for the detection of potentially weak CO emission. To accomplish this, in this study we correct for stellar absorption features in the composite (star + disk) spectra of our sample.

With this method, we are also sensitive to weak continuum excesses (continuum veiling) which are a measure of warm dust close to the star. Although veiling is well studied at shorter wavelengths, the $5\mu\text{m}$ region has received less attention (Najita et al. 2008; Salyk et al. 2009). The use of CO as a probe of residual gas in TOs and WTTS complements other related studies that use mid-infrared H_2 lines (e.g., Pascucci et al. 2006), UV H_2 features (Ingleby et al. 2009, 2012; France et al. 2012), and other mid-infrared diagnostics (Pascucci et al. 2007; Najita et al. 2010) as *in situ* tracers of residual gas.

Our M -band spectroscopic observations and data reduction are described in §2. The modeling technique and analysis is described in §3, and the results reported in §4. We discuss our findings in §5 and conclusions in §6.

2. Observations

For our study of the dissipation of gas and dust in the inner disks of TOs and WTTS, we selected a small sample of well characterized TOs and WTTS in Taurus and the TW Hydra Association (TWA). The average age of the sources in these regions (few Myr for Taurus and ~ 10 Myr for TWA) spans the expected gas dissipation timescale. Because our gas diagnostic, CO ro-vibrational emission, is known to decline in strength with stellar accretion rate at high \dot{M}_* (Najita et al. 2003), we also studied a small sample of CTTS with low \dot{M}_* in order to determine if CO remains a reliable gas diagnostic at low \dot{M}_* . Our sample (Table 1) includes 4 CTTS with relatively low accretion rates ($\sim 10^{-9} \text{M}_\odot \text{yr}^{-1}$; IP Tau, DN Tau, V836 Tau, ZZ Tau, Najita et al. 2015; Valenti et al. 1993), 5 well-studied transition objects (TW Hya, UX Tau A, LkCa 15, GM Aur, CoKu Tau/4, Furlan et al. 2006) and 15 WTTS (Furlan et al. 2006, 2011). The targets span a range in spectral type (K0-M3; Table 1). The majority of the sample are apparently single stars. ZZ Tau and Coku Tau/4 are 0.06 arcsec binaries (Schaefer et al. 2006; Ireland & Kraus 2008). Hubble 4, HBC 427, V827 Tau, and TWA 5 are spectroscopic binaries (Walter et al. 1988; Neuhäuser et al. 2001; Kraus et al. 2011; Mahmud et al. 2011).

The data were obtained over multiple observing runs from 2001 January, 2003 January, 2005 February, and 2007 January (Table 1). We took M -band spectra of the Taurus and TWA objects in our sample using the Keck II facility spectrometer, NIRSPEC (McLean et al. 1998) at the summit of Mauna Kea. We obtained multi-order spectra at high resolution ($R=25,000$ and $R=18,500$), with echelle and cross-disperser gratings oriented to give spectral coverage spanning $4.586 - 4.662 \mu\text{m}$ (order 16) and $4.890 - 4.972 \mu\text{m}$ (order 15). Depending on the seeing conditions, the $0.432'' \times 24''$ slit or $0.576'' \times 24''$ slit was used to acquire spectra through the M-wide broadband filter, imaging echelle orders 15, 16 and 17 onto the 1024×1024 Aladdin-3 detector.

The large thermal sky background required short exposure times (1 – 2 sec) for all our targets, and were co-added internally (20 – 60 times). The telescope was noddled $\pm 6''$ along the slit in an ABBA pattern to obtain simultaneous source and sky spectra at each nod position. Spectra of early type standards were taken at similar airmass for removal of telluric absorption lines in the targets. Spectra of flux standards were taken through the widest available slit (5 pixels, $0.720''$) for spectroscopic flux calibration. High signal-to-noise flat fields for the M -band were obtained by combining multiple (i.e., 20) continuum lamp images of short exposure time (1 sec), taken with the NIRSPEC internal calibration unit.

The data were reduced by Nathan Crockett following the procedure described in §2 of Najita et al. (2008) using IRAF packages (Massey et al. 1992, 1997). Exposure frames from nod pairs were dif-

ferenced then divided by a normalized flat field image. Using spatially resolved telluric emission sky lines present in each exposure, the images were rectified to create mono-spectral columns and mono-spatial rows, which allowed a large background aperture to be used when extracting the spectral trace of the source, producing a higher signal-to-noise spectrum. Rectified images from each beam position were shifted, as needed, to place the peak of each source aperture on the same pixel before co-adding them.

Spectra of target and telluric calibration stars were extracted from an aperture profile having a width of ± 2 pixels ($\pm 0.39''$) about the spatial peak and subtracted by a background aperture that was more than 7 pixels ($1.35''$) from the source peak on both sides, spanning a total width of ~ 40 pixels ($\sim 7.8''$). Telluric absorption features were removed by dividing extracted target spectra by the normalized telluric spectra taken at similar airmass.

Our CTTS and TO target spectra were flux calibrated from corresponding telluric star observations that were taken close in time. Except in three cases (i.e., UX Tau A in 2005, V836 Tau in 2003, and IP Tau), wide slit (i.e., $0.72''$) observations were unavailable or were of insufficient signal-to-noise. Instead, narrower slit observations (i.e., $0.43''$) for both target and telluric standard were used for flux calibration under the assumption of equal slit losses. In some cases, a comparison of summed counts between different nod positions within a given target or telluric observation sequence differed by more than 15%. Consequently, the errors in the flux calibration of GM Aur, DN Tau, TW Hya (in 2001), IP Tau, V836 Tau (in 2003), and LkCa 15 (in 2001) are dominated by uncertainty in the flux throughput caused by variable slit losses in the target and telluric observations.

To correct for the broad $\text{Pf}\beta$ absorption at $4.650\mu\text{m}$ in our early-type telluric standards, we created a spline fit to the $\text{Pf}\beta$ feature in the spectrum of the telluric standard and then multiplied the fit into the (telluric-corrected) target spectrum to restore its true continuum shape (Fig. 1).

3. Analysis

Weak fundamental CO line emission from the warm inner disk can be obscured in the composite (star + disk) spectrum by CO absorption lines from the stellar photosphere. Thus we need a template of the pre-main-sequence stellar photosphere in order to accomplish our goals of (i) detecting and measuring potentially weak CO emission from the disk and (ii) measuring the excess emission over the stellar photosphere, i.e., the veiling at M -band (r_M). Because it is difficult to obtain a complete set of observational templates (i.e., high signal-to-noise spectra of disk-less PMS stars that span the range in T_{eff} , $\log g$, and $v \sin i$) in our sample, we created synthetic spectral templates with the appropriate properties for each source.

3.1. Spectral Fitting Method

We used MOOG (Snedden 1973) to generate synthetic M -band stellar spectra for these sources following the procedure detailed in Najita et al. (2008). The inputs to MOOG are a model atmosphere for a given effective temperature and gravity, rotational and instrumental broadening, microturbulence, and a limb darkening coefficient. We used the Allard NG 5.0 model atmospheres (Hauschildt et al. 1999), formatted to run as input to MOOG. We also assumed solar abundances, consistent with stellar abundance measurements of nearby star forming regions (Padgett 1996; Santos et al. 2008), and stellar rotational velocity broadening values from the literature (Table 1), convolved with the instrumental broadening of our slit resolution. We adopted a limb darkening coefficient of 0.6, a microturbulence of 0.5 km s^{-1} , and theoretically calculated oscillator strengths for ^{12}CO and ^{13}CO transitions (Goorvitch 1994) to generate model CO stellar absorption spectra.

Effective temperature (T_{eff}) and surface gravity ($\log g$) are the primary input parameters for the spectral synthesis. Because veiling and $\log g$ have a similar effect on our $4.7\mu\text{m}$ spectra, we were unable to measure $\log g$ from our spectra themselves. We therefore used literature values to determine the input $\log g$ and T_{eff} (Table 1) and then fit for veiling. The uncertainties in the resulting effective temperatures are typically $\Delta T_{\text{eff}} \sim 150\text{K}$ (~ 1 spectral subclass). At a fixed gravity of $\log g = 4.0$, which is typical for our sample, the uncertainty in T_{eff} corresponds to a typical uncertainty in the veiling of $\Delta r_{\text{M}} \sim 0.05$. For most of our sources, we estimated $\log g$ using stellar luminosities and temperatures or spectral types from the literature, and theoretical evolutionary model tracks (Table 1).

We adopted the spectral types, luminosities, and masses of Herczeg & Hillenbrand (2014) with a few exceptions. For V410 Tau, which was not included in that study, we used the effective temperature and luminosity from Kenyon & Hartmann (1995) and Bertout et al. (2007). The luminosity was converted to gravity using the stellar mass derived from the model tracks of Baraffe et al. (2015). We also adopted T_{eff} and $\log g$ values from spectroscopic fits when available (Balachandran & Carr 1994; Johns-Krull et al. 2004, UX Tau A, LkCa 19, and Hubble 4). Errors on the luminosity and derived temperature values corresponded to a typical range of ± 0.15 in $\log g$. Using the Siess et al. (2000) tracks instead would result in lower gravities by ~ 0.05 in the log.

For TW Hya, we adopted the temperature and gravity reported by Yang et al. (2005) from detailed modeling of high resolution, high signal-to-noise spectra. For TWA 10, we adopted the spectral type from Webb et al. (1999) and estimated its gravity from the bolometric luminosity of de la Reza & Pinzón (2004) and the mass predicted by Baraffe et al. (2015, Table 1).

Uncertainties in the photometry, distance, and position of theoretical tracks yielded an uncertainty in the inferred gravity of $\Delta \log g \sim \pm 0.35$. Across the temperature range of ($T_{\text{eff}} = 3400\text{--}4400\text{K}$), characteristic of many of our sources, the uncertainty in the surface gravity gives an uncertainty of order ($\Delta r_{\text{M}} \sim \pm 0.15$) in the veiling. Generally, the increasing strength of the CO absorption lines in synthesis models with decreasing temperature and/or decreasing gravity is offset with increased veiling.

Since the input model atmosphere structures for our synthetic spectral modeling were more coarsely gridded in T_{eff} ($\Delta T_{\text{eff}} = 100\text{K}$ for $T_{\text{eff}} < 4000\text{K}$, and $\Delta T_{\text{eff}} = 200\text{K}$ for $T_{\text{eff}} \geq 4000\text{K}$) and $\log g$ ($\Delta \log g = 0.5$) than the values we used from the literature, we chose the nearest model value in each case (see Table 2). Rotational broadening and radial velocity could be determined directly from our model fits, and our observations confirmed values reported in the literature, except in a few cases (Table 2). For each source, we used the $v \sin i$ velocity broadening value from the literature (Nguyen et al. 2012; Yang et al. 2005, 2008; Johns-Krull et al. 2004; White & Hillenbrand 2004; de la Reza & Pinzón 2004; Reid 2003; Torres et al. 2003) in the model fits unless a better fit value could be obtained (Table 1).

To validate the models, we first fit the spectra of two main sequence dwarf standards with well-known stellar parameters (i.e., effective temperature, surface gravity, abundances) that were observed with the same instrumental setup as our sources. We found a good fit to the observed spectra (Fig. 2) using a model with the known stellar parameters of 61 Cyg A and B: K5V and K7V spectral types respectively, a gravity of $\log g = 4.5$, which is appropriate for a dwarf luminosity class of a late-type main sequence star and is consistent with interferometric radius measurements (Kervella et al. 2008), and a metallicity of $[\text{Fe}/\text{H}] = -0.27$ (Luck & Heiter 2005). As we expected for these normal main sequence stars, we found the best fit veiling value to be consistent with zero, after testing for negative and positive values of veiling.

We also fit the spectrum of a late-type dwarf standard (M0V) observed in a nearby spectral region (HD 79211, Salyk private communication; see also Salyk et al. 2009), using a model with a temperature ($T_{\text{eff}} = 3800\text{K}$) and gravity ($\log g = 5.0$) expected for this main sequence star. We find that the model fits the observed standard very well with zero veiling, as expected.

3.2. Measured Veiling and CO Emission

We determined the M -band continuum veiling of our sources by fitting their observed spectra with a sum of an appropriate synthetic stellar template (§3.1) and a featureless veiling continuum with a strength r_{M} times the stellar continuum. The best-fitting value of r_{M} was determined using the RMS pixel-to-pixel fit in selected sub-regions in our spectra that had telluric transmission $\geq 80\%$ and were free of both artifacts and circumstellar CO and $\text{Pf}\beta$ emission. Veiling values $r_{\text{M}} \simeq 0\text{--}5$ were obtained (Table 2). To estimate the uncertainty in r_{M} due to the uncertainty in T_{eff} ($\pm 150\text{K}$) and $\log g$ (± 0.25), we considered pairs of T_{eff} and $\log g$ values within the allowed range that maximized or minimized the strength of the stellar absorption lines in our templates and fit for the corresponding values of r_{M} . We adopted the range in the fit values as our uncertainty in r_{M} (Table 2). Generally, the WTTS in our sample show little or no veiling (e.g., Fig. 3a), while the CTTS have significant M -band veiling (e.g., Fig 3c).

We expect the veiling to be underestimated if one uses a main sequence stellar template to fit pre-main sequence sources. To illustrate this point, we can look at possible model fits to

CoKu Tau/4, a source with a gravity that is typical of the pre-main-sequence sources in our sample, $\log g \sim 4.2$. Because this value falls between the $\log g$ values sampled by our atmosphere models ($\log g = 4.0, 4.5$, and 5.0), we adopted a model with the closest gravity $\log g = 4.0$, for which the best fit veiling is $= 0.3$ (Fig. 3b).² If we had used a model with main sequence gravity (i.e., $\log g = 5.0$ and $T_{\text{eff}} = 3800K$) or an equivalent main sequence star as a template (e.g., HD 79211 Salyk et al. 2009), we would have inferred a lower veiling value of $r_M = -0.1$. Thus, using spectral synthesis templates enables a closer match in $\log g$ and T_{eff} , enabling the identification of weak continuum veiling.

Although weak CO emission can be obscured by stellar CO absorption features, it can be unveiled by correcting for the veiled stellar continuum. To search for weak CO emission, we subtracted the synthetic veiled stellar spectrum and replaced it with a featureless continuum of the same strength. We then measured any detected CO and Pf β emission.

Table 3 reports measured CO emission equivalent widths and $1\text{-}\sigma$ upper limits relative to the total (stellar + veiling) continuum. The upper limits include contributions from pixel-to-pixel noise and the uncertainty in the determination of the continuum level. The CO equivalent widths reported in Table 3 were multiplied by the continuum flux at the middle of the corresponding order ($4.63\mu\text{m}$ or $4.93\mu\text{m}$) to obtain CO emission fluxes. For the WTTS, whose spectra were not flux calibrated (§2), we first estimated their flux at the center of the M -band from their K -band magnitudes in the literature and assuming main sequence K – M colors (Kenyon & Hartmann 1995) appropriate for their spectral type. We then used the spectral shape of IP Tau through the M -band as a template to estimate the WTTS fluxes at $4.6\mu\text{m}$ and $4.9\mu\text{m}$. The spectral shape for IP Tau was obtained from the flux calibrated measurements reported here, which had appropriate wide slit observations at high signal-to-noise.

4. Results

We detect 1-0 ^{12}CO emission from 7 of the 24 sources in our sample (Fig. 4, Table 3): all of the non-binary, low accretion rate CTTS (DN Tau, IP Tau, V836 Tau) and all of the non-binary TOs (GM Aur, LkCa 15, TW Hya, UX Tau A). For the detected CO emission sources, we constructed average CO line profiles (Fig. 5) for both R-branch (red) and P-branch (blue) lines by interpolating individual lines onto a common velocity grid and averaging the emission, excluding regions of poor telluric correction or other artifacts. Table 3 lists the lines that were included in the average profiles along with their resulting FWHM and equivalent widths. When CO emission is detected, the emission profiles are symmetric and centered within 4 km s^{-1} of the stellar velocity, as reported in the literature. (Fig. 5).

²While we could interpolate between model fits to obtain a more precise value (i.e., since the $\log g = 4.5$ model requires a veiling of $= 0.1$, the veiling for $\log g = 4.2$ is close to $r_M = 0.2$), it would not alter the results reported here. As a result, we report instead the properties inferred using the model with the closest $\log g$ and T_{eff} .

We also detect $\text{Pf}\beta$ emission in 2 sources (TW Hya, GM Aur), with 4 others (LkCa 15, UX Tau A, IP Tau, DN Tau) showing marginal detections (Fig. 6). The $\text{Pf}\beta$ emission detected from GM Aur and TW Hya in 2001 and 2003 had equivalent widths of 24\AA , 34\AA , and 63\AA , and FWHM of 206 km s^{-1} , 99 km s^{-1} , and 95 km s^{-1} , respectively.

Assuming that the CO emission arises in a Keplerian disk (Salyk et al. 2011; Brittain et al. 2007; Najita et al. 2003; Banzatti & Pontoppidan 2015), the broad line profiles of the low accretion rate CTTS (K7/M0; $120\text{--}150\text{ km s}^{-1}$ FWHM) indicate that most of the CO emission from these sources arises close to the star, within 0.5 AU, given their system inclinations (Andrews & Williams 2007; Ardila et al. 2013; Najita et al. 2008) and stellar masses (Andrews et al. 2013) from the literature. The narrower line profiles of the CO emission from the TOs ($10\text{--}80\text{ km s}^{-1}$ FWHM, deconvolved) imply that their CO emission arises from larger radii (0.3–2 AU) given their higher average masses (corresponding to their K2–K7 spectral types; Andrews et al. 2013) and system inclinations (Andrews et al. 2011a; Pontoppidan et al. 2008).

Salyk et al. (2009) reached the same conclusion in their study, which included the same TOs studied here (see also Banzatti & Pontoppidan 2015). Similar in spirit to these results, Hoadley et al. (2015) found that the line profiles of UV fluorescent H_2 emission from TOs is narrower than those of classical T Tauri stars, with the narrower profiles implying inner emission radii ~ 4 times larger on average than for classical T Tauri stars. We confirm that this conclusion also holds when the CO line widths of TOs are compared to the CO line widths of CTTS with similar accretion rates. A similar trend has also been found for the [OI] emission width from TOs. In the study of Simon et al. (2016), three of the four TOs studied lack a broad [OI] low velocity component, suggesting that the emission arises from gas further away from the star than the [OI] emission from CTTS.

The inferred CO emission radii for the TOs are well within the sub-millimeter cavity for these sources (radii of 2 AU, 25 AU, 28 AU, 50 AU for TW Hya, UX Tau A, GM Aur, and LkCa 15, respectively; Andrews et al. 2016, 2011b). The presence of gas within the sub-millimeter cavity is consistent with the results of previous studies of CO emission from transition objects (Rettig et al. 2004; Najita et al. 2008; Salyk et al. 2007, 2009; Pontoppidan et al. 2008) and the ongoing stellar accretion in these systems, which also indicates gas close to the star.

As shown in Tables 2 and 3, all of the sources from which CO emission is detected have significant veiling ($r_M > 0.5$) and measurable accretion. CO emission is not detected from WTTS and non-accreting transition objects (CoKu Tau/4). Our results are similar to those of Salyk et al. (2009, 2011) who found that CO emission is detected from some but not all transition objects. In several sources we detect apparent non-zero M -band veiling ($r_M \geq 0.3$) but no CO emission. One of these sources, TWA 7, also has a detected continuum excess at longer wavelengths with *Spitzer* (Low et al. 2005). The lack of accompanying tracers of a gas disk is consistent with the suggestion that the continuum excess arises from collisional debris produced through planet building. Although the WTTS V819 Tau also has a reported excess at *Spitzer* wavelengths (Furlan et al. 2009), we did

not measure an M -band excess for this source (Table 2). The TWA 2AB binary, which is spatially unresolved in our spectrum, has components with similar spectral types (M1.7 and M3.5 for A and B, respectively) and a luminosity ratio of 3.4 (Herczeg & Hillenbrand 2014). If all of the veiling is associated with the A component, the veiling we measure ($r_M = 0.4$) only slightly underestimates the veiling of the A component ($r_M = 0.5$).

We measure M -band veilings of $r_M = -0.2$ to 0.4 for our WTTS sources and $r_M = 0.3$ to 5.1 for transition objects (Table 2). Negative veiling values may result if the literature values of T_{eff} and $\log g$ are not quite right and/or from the finite gridding in T_{eff} and $\log g$ of the model atmospheres. The difference between our inferred veiling for CoKu Tau/4 of $r_M = 0.3$ and the smaller value from Salyk et al. (2009) results from the lower gravity stellar template used in our study. The lower gravity of CoKu Tau/4 increases the strength of its stellar CO absorption lines compared to a main sequence star of the same spectral type, which is compensated for by modest ($r_M = 0.3$) continuum veiling. As a result, the strength of the CO absorption features are similar for the main sequence standard and the (veiled) spectrum of CoKu Tau/4. Future observations that enable more precise values of $\log g$ (e.g., more precise distance estimates) will allow us to determine r_M more precisely.

Figure 7 plots r_M against the $24\mu\text{m}/K_s$ flux ratio for our sample (Low et al. 2005; Rebull et al. 2010; Furlan et al. 2006, 2011). Transition objects with large $24\mu\text{m}/K_s$ flux ratios (1–6) have a range of r_M (0.3–5), whereas WTTS are clustered toward small excesses on both axes. The low accretion rate T Tauri stars in our sample have intermediate $24\mu\text{m}/K_s$ colors (0.4–1) and span the same range of r_M as the TOs. The high r_M for the transition objects LkCa 15 and UX Tau A is consistent with their classification as “pre-transition disks”, systems with transition disk SEDs that also have a significant near-infrared excess indicative of an optically thick inner disk (Espaillat et al. 2010).

For objects studied at 2 epochs, we can compare any variation in the CO flux and M -band veiling flux, which were measured simultaneously. Figure 8 plots the measured CO equivalent widths against r_M (Tables 2 and 3) for all sources. Because the CO equivalent width is multiplied by $(1 + r_M)$, this product represents the CO emission flux ratioed to the M -band stellar continuum flux. Thus the two axes show the continuum excess and the CO emission flux relative to the stellar continuum. Dashed lines connect sources observed at more than one epoch. For LkCa 15 and TW Hya, which have multiple measurements, we find an increase (decrease) in the continuum excess is accompanied by an increase (decrease) in the CO emission flux. These variations could result from increased accretion, which can increase the column density of the gas and dust in the inner disk and/or raise the temperature of the emitting gas. However, for two other sources, a change in r_M (UX Tau A) or CO emission strength (V836 Tau) was not accompanied by a significant change in the other quantity. Figure 8 also shows that some transition objects can have higher M -band veiling than the low accretion rate T Tauri stars (e.g., LkCa 15), and that the transition objects have systematically lower CO emission flux than low accretion rate T Tauri stars with the same M -band veiling.

Figure 9 compares measured CO emission fluxes with stellar accretion rates from the literature, for both the sample studied here (large symbols) and sources from the literature (small symbols) (Brown et al. 2013; Najita et al. 2003, 2007; Natta et al. 2006; Valenti et al. 1993; Espaillat et al. 2010; Eisner et al. 2005). The CO fluxes are normalized to a distance of 140 pc, assuming distances of 140 pc for Taurus sources, 120 pc for Oph sources, and 56 pc for TWA sources. CO emission strength generally increases with stellar accretion (see also Najita et al. 2003; Brittain et al. 2003), although there is significant dispersion. The transition objects studied here cluster in the lower left region of the plot, i.e., they have low CO emission fluxes for their stellar accretion rates.

WTTS show no CO emission down to equivalent widths of $\sim 0.1\text{\AA}$ and fluxes of 10^{-19} W m^{-2} . The upper limit on the CO emission flux for Hubble 4 is particularly large because it is very bright. The WTTS accretion rate upper limits shown in Figure 9 are fiducial limits based on the work of Manara et al. (2013) who estimated the limit on measurable stellar accretion that is imposed by typical levels of stellar chromospheric emission. The limiting values depend on stellar mass and age. Thus we use individual masses, as derived from the gravities (Table 1), and representative ages for TWA (i.e., 10 Myr) and Taurus (i.e., 2 Myr) to estimate the accretion rate upper limits for the WTTS in our sample.

5. Discussion

5.1. CO Emission and M -band Excess from Transition Objects

We find that CO ro-vibrational emission generally declines with decreasing stellar accretion rate (Fig. 9). CO emission also declines from CTTS to TO to WTTS classes, with an overlapping spread in emission strength in the CTTS and TO classes. Transition objects have lower CO emission flux than TTS with similar stellar accretion rate (Fig. 9) or similar M -band veiling (Fig. 8). They also have narrower CO emission line profiles than CTTS with similar accretion rates and inclinations (see also Salyk et al. 2009).

Although we generally expect gas and dust diagnostics to be related, the lack of a strong correlation between r_M and CO emission flux in our sample (Fig. 8) is not all that surprising, because r_M and CO emission are affected by distinct processes. While M -band veiling should increase linearly with dust mass when the dust disk is optically thin, other effects enter when the dust is optically thick. Dust scale heights can vary from source to source depending on the gas temperature and the extent of grain settling out of the atmosphere, and shadowing effects can come into play (e.g., Espaillat et al. 2011). In parallel, CO emission strength can depend on factors other than total gas mass, e.g., gas temperature, CO abundance, and optical depth. The scatter seen in Figure 8 could be due to differences in some of these same factors among sources with similar accretion rates.

Interestingly, some of the transition objects are mixed in with the CTTS in Figure 9. SR24 S

and DoAr 44 (open gray circles), both located in Ophiuchus, have some unusual properties as transition objects. SR24 S is identified as transition object based on the inner cavity in its sub-millimeter continuum emission (Andrews et al. 2011b) rather than by its SED. Its SED is unremarkable and is consistent with an inner disk that is optically thick in the near- and mid-infrared. DoAr 44 has a more typical transition object SED, with a mid-infrared “dip” (Espaillat et al. 2010), although it is unusual in that it has a rich molecular emission spectrum at *Spitzer* wavelengths (Salyk et al. 2015). The strong CO emission from these two sources is consistent with the evidence for substantial small dust grains (SR24 S) and substantial gas (DoAr 44) close to the star.

In contrast to these two sources, the CO emission from the rest of our TO sample is weaker than that from CTTS of the same r_M or stellar accretion rate (Fig. 8, open triangles in Fig. 9). The reduced CO emission strength of TOs compared to CTTS could result from a reduction in the CO abundance, emitting area, or temperature of the gaseous disk, or some combination of these.

Reduced CO abundance. The weaker mid-infrared excess of TOs compared to CTTS has been interpreted as evidence for a reduced grain abundance in their inner disks, possibly as a consequence of planet formation. The accumulation of grains into larger objects (such as rocks, planetesimals, and protoplanets) will reduce the grain abundance in the inner disk. A similar result could occur when a giant planet forms and opens a gap at large disk radii (beyond the CO emission region), and the resulting pressure bump at the outer edge of the gap filters out grains from the material reaching the inner disk (Rice et al. 2006; Zhu et al. 2012). In disks with a highly reduced grain abundance, CO may form less efficiently because the formation of the precursor molecule H_2 on grain surfaces is less efficient (see section 5.2). The resulting CO abundance may be suppressed more strongly close to the star, for a given grain reduction factor, because of the higher rate of photodestruction at smaller disk radii. This effect would favor CO emission from larger disk radii, resulting in smaller CO emitting areas and narrower CO line profiles (as in Fig. 5 and Salyk et al. 2009).

Reduced gas emitting area. Another possibility is that the weaker CO emission from TOs reflects a smaller emitting area for the gaseous inner disk as whole, not just the radial extent of the region where CO is abundant. In the Simon et al. (2016) study of [OI] emission from TTS, the FWHMs of the [OI] and CO lines are very similar for the 3 TOs where both lines are detected (GM Aur, UX Tau4, TW Hya). The similar [OI] and CO line profiles may suggest that both the atomic and molecular gas are similarly restricted to larger radii than in CTTS disks, as in a truncated gaseous disk. Because TOs have significant stellar accretion rates, gas from the disk clearly reaches the star. A giant planet located close to the star can truncate the inner disk and concentrate the gas in accretion streams, reducing the gas emitting area. Because the CO emission from CTTS arises close to the star ($\lesssim 0.3$ AU; Salyk et al. 2011; Najita et al. 2003), a planet would likely have to be located within an AU to impact the CO-emitting region of the disk. The narrower CO emission profiles of TOs, compared to those of CTTS with similar accretion rates and inclinations, suggests that any truncation of the CO emission occurs from within (rather than beyond) the emission region, i.e., it requires a planet at ~ 0.1 AU, similar to the close-in giant

planet that is reported to orbit V830 Tau (Donati et al. 2016).

Any planet capable of affecting the structure of the gas in the CO-emitting region would be distinct from the giant planets that could create the much larger inner holes inferred for the TOs in our sample, i.e., TOs would be multiple planet systems (Zhu et al. 2011; Dodson-Robinson & Salyk 2011). The planet that creates the inner hole would be located far from the CO emission region, near the inner hole radius (2 AU, 28 AU, 25 AU, 50 AU for TW Hya, GM Aur, UX Tau A, and LkCa 15; Andrews et al. 2011b, 2016), as imaged directly in one case (LkCa 15b at 14.7 AU; Kraus & Ireland 2012; Sallum et al. 2015).

If a high mass (giant) planet is needed to truncate the disk close to the star, such planets are rarer among mature sun-like stars than TOs are among young stars. Hot Jupiters ($P < 10$ d; $M \sin i > 0.1 M_J$) are present in $\sim 1\%$ of sun-like stars (Wright et al. 2012), whereas TOs represent 10–15% of the disk-bearing population of young stars (Muzerolle et al. 2010; Espaillat et al. 2014). The low incidence rate of hot Jupiters around mature sun-like stars seems to argue against this interpretation.

This scenario is more plausible if the same dynamical effect can be achieved with lower mass planets, which are more common as close companions to sun-like stars. Along these lines, (Andrews et al. 2016) have suggested that a young super-Earth (several M_E) may be responsible for the narrow gap observed in the inner 1 AU of the TW Hya disk.

Reduced gas temperature. Alternatively, TOs may show weak CO emission as a result of reduced gas temperature in the inner disk (see also Banzatti & Pontoppidan 2015). The lower accretion rates of TOs lead to reduced UV irradiation and *in situ* mechanical heating, both of which are driven by accretion (e.g., Ádámkovics et al. 2016, and references therein), potentially reducing the column density of the warm disk atmosphere. The detectable CO emission of the low accretion rate CTTS, which have accretion rates similar to that of the TOs, implies that this scenario requires more than a reduced accretion rate to explain the reduction in CO emission.

Empirically, the CO emission of the TOs in our sample does not appear to be much cooler than that of CTTS. Like the low accretion rate CTTS, the TOs LkCa 15 and GM Aur have low-J and high-J lines of comparable equivalent width (Fig. 5). Only UX Tau A has stronger low-J lines than high-J lines signaling an unusually low temperature. Salyk et al. (2009) previously noted that TOs typically do not show high-J lines, contrary to our results. The difference might be due to the range of J sampled in our respective spectral settings. Our high-J lines are slightly lower in excitation than those studied by Salyk et al. (2009).

As a variant of this idea, shadowing effects might reduce the irradiation heating of the disk atmospheres of TOs and decrease their CO emission. Along these lines, Espaillat et al. (2011) have noted a “see-saw” behavior in the variability of pre-transition disks (a subset of TOs): when the near-infrared excess increases, the mid-infrared excess decreases. Espaillat et al. (2011) can reproduce this behavior, observed for LkCa 15, UX Tau A, and IP Tau, by changing the height of the inner disk edge near the dust sublimation radius (at ~ 0.1 AU) by $\sim 22\%$, 17% , and 17%

respectively. When the height of the inner disk edge is larger, the emission at the wavelengths where the inner disk edge dominates the emission ($2 - 8\mu\text{m}$) is higher and casts a larger shadow on the outer disk. Reduced irradiation heating of the shadowed region would reduce the column of warm CO-emitting gas. The changing height of the inner disk edge can be driven by varying accretion: a higher accretion rate raises the surface density of the inner disk, which increases both the IR excess and the height at which the inner edge of the disk becomes optically thick to stellar radiation.

Some of the properties of the TOs in our sample are consistent with shadowing; i.e., the narrow CO line profiles of the TOs locate the emission at larger radii than the dust sublimation radius. For LkCa 15 and UX Tau A, the HWHM of their CO emission corresponds to emitting radii of 0.35 AU and 2.5 AU respectively given their stellar masses ($1.05M_{\odot}$ and $1.58M_{\odot}$; Andrews et al. 2013) and inclinations ($i = 49$ and $i = 35$, respectively; Andrews et al. 2011b), larger than the radius of the inner disk edge. However, the HWHM of the CO emission from GM Aur also corresponds to a large emitting radius of 2 AU given its stellar mass ($1.35M_{\odot}$; Andrews et al. 2013) and inclination ($i = 56$; Andrews et al. 2011b) despite the lack of an optically thick inner disk edge that could possibly produce any shadowing. In addition, the variability seen in Figure 8 is inconsistent with the shadowing scenario. When r_M increases significantly (which would correspond to the increasing height of the inner disk edge in this scenario), the CO emission is either unaffected (UX Tau A) or increases rather than declining as a result of greater shadowing (LkCa 15).

To summarize, it seems plausible that the reduced CO emission from TOs results from chemical and/or dynamical effects. The low grain abundance of the inner disk of TOs is likely to reduce the abundance of CO close to the star, reducing the strength of the CO emission. Low mass planets located within 0.3 AU of the star may also open narrow gaps in the inner disk, reducing the CO emitting area. Detailed thermal-chemical models of disk atmospheres with low grain abundances and studies of the impact of low mass planets on inner disks are needed to further explore these interpretations.

5.2. Residual Gas in WTTS Disks?

To explore whether our results place any useful constraints on the lifetime of gaseous inner disks, we need to understand how our upper limits on CO emission strength translate into corresponding upper limits on gas mass. An important issue is how the CO abundance in the disk is affected by a diminishing grain abundance and whether the CO that remains in the disk is hot enough to emit detectable ro-vibrational emission.

While CO could be dissociated more readily when the inner disk has less dust to shield the gas from dissociating stellar UV irradiation, processes such as molecular self-shielding and the reformation of CO can help to maintain a significant reservoir of CO even when grains are greatly reduced in abundance (Bruderer 2013; Ádámkovics et al. 2014, 2016). H_2 is an important precursor

molecule for the formation of CO. In the absence of grains, H_2 may form on PAHs (Bruderer 2013) or through gas phase processes (Glassgold et al. 2009). Therefore, CO might persist in the inner disk even in a disk with low continuum opacity.

Because multiple factors beyond gas column density affect the CO abundance and temperature (UV luminosity, grain abundance, PAH abundance), we would ideally rely on theoretical models of the thermal-chemical properties of dissipating disks for insight. Unfortunately, these models are in their infancy and general models for low mass stars are not available. Gorti et al. (2011) studied the specific case of TW Hya. Bruderer (2013) has primarily focused on Herbig stars.

In the absence of general models for T Tauri stars, we use the Bruderer (2013) models to illustrate how our results could be used to constrain the residual gas in WTTS when appropriate models are available. On the one hand, the high FUV luminosity of the Herbig model (and resulting photodissociation) tends to underestimate the disk CO abundance. On the other hand, the high (ISM) PAH abundance that is assumed (a mass ratio of 5% relative to dust) tends to increase the CO emission because of the role of PAHs in absorbing UV photons, heating the gas through the photoelectric effect, and as an additional pathway for H_2 formation. While PAHs have been found to be present in the dust cavity of one Herbig system (IRS 48; Geers et al. 2007), their abundance in T Tauri disks is uncertain.

In the Bruderer (2013) reference model for a transition disk, the inner region of the disk is reduced in dust abundance (or column density) by a factor of 10^{-5} relative to its original value. The original disk has a gas mass column density of 1700 g cm^{-2} at 0.5 AU and a dust mass column density of 17 g cm^{-2} at 0.5 AU. The value of the decrement is consistent with observations of transition disks. Andrews et al. (2011b) reports decrements of $\sim 10^{-5} - 10^{-6}$ for transition disks at sub-millimeter wavelengths.

Despite the large FUV luminosity of the reference model ($0.7L_\odot$), CO survives in the inner disk. When the gas column density is reduced by a factor of 100 relative to its original value (to $\sim 17 \text{ g cm}^{-2}$ at 0.5 AU), the gas reaches a temperature of $\sim 1000 \text{ K}$ and a density $\sim 10^{11} \text{ cm}^{-3}$, and the disk is expected to produce CO emission (Fig. 4 of Bruderer 2013). This is consistent with our observations: we do see CO emission from transition disks with M -band excess.

Bruderer (2013) also presents results for systems with even larger decrements in the dust abundance. When there is no dusty inner disk (in the model the dust is reduced by a factor of $\delta_{\text{dust}} = 10^{-10}$), the CO abundance remains high at the disk mid-plane ($x_{\text{CO}} = 10^{-4}$) for a decrement in the gas disk of $\delta_{\text{gas}} = 10^{-4}$ or a gas column density of 0.17 g cm^{-2} at 0.5 AU). The CO in the mid-plane is hot ($\sim 1000 \text{ K}$) because of the lack of dust-gas cooling and the mid-plane is dense $\sim 10^{12} \text{ cm}^{-2}$ (from Fig. 4 of Bruderer [2013], scaling down to the mid-plane). As a result, the CO column within 1 AU ($10^{17} - 10^{18} \text{ cm}^{-2}$) is likely to produce CO ro-vibrational emission.

When the gaseous disk has an even lower column density, (i.e., $\delta_{\text{dust}} = 10^{-10}$, $\delta_{\text{gas}} < 10^{-4}$), there is no substantial CO reservoir in the inner disk ($N_{\text{CO}} < 10^{14} \text{ cm}^{-3}$; see also Fig 8 of Bruderer 2013). Using these models as a guide, we would not expect to see CO ro-vibrational emission for

dust-free disks with gas column densities $\lesssim 0.17 \text{ g cm}^{-2}$ at 0.5 AU. A better estimate for the limiting gas column for detectable CO ro-vibrational emission could be made with models that are more closely tailored to the properties of T Tauri disks and which explore the sensitivity of the results to PAH abundance.

If our WTTS observations truly indicate a gas column density limit of $< 0.17 \text{ g cm}^{-2}$ at 0.5 AU, they help to constrain the impact of residual gas on the eccentricities of forming planets. Gravitational interactions between planets and the gas damp eccentricity and inclination (Kominami & Ida 2002; Agnor & Ward 2002). As a result, in closely packed planetary systems, a residual gas disk may play a role in suppressing planet-planet interactions and scattering (Alexander et al. 2014). Kominami & Ida (2002) suggested that residual gas in the terrestrial planet region at the level of $10^{-3} - 10^{-4}$ of the MMSN could circularize the orbits of terrestrial planets on timescales of ~ 10 Myr (in the absence of secular perturbations by giant planets; Kominami & Ida 2004), potentially producing the low eccentricities observed in the solar system. If the Solar System planets formed in a disk like the WTTS systems studied here, gas drag would be unable to circularize the planets in ~ 10 Myr because little gas remains in the disk ($< 10^{-4}$ of the MMSN) at ages $\lesssim 10$ Myr. More dilute reservoirs of gas ($< 10^{-4}$ of MMSN), beyond our ability to probe, could reduce exoplanet eccentricities on longer timescales.

The lack of evidence for residual gas disks surrounding the WTTS, as traced by CO in our sample (age 1–2 Myr for Taurus and ~ 10 Myr for TWA) does not help to explain the slow rotation rates of older stars (see Bouvier et al. 2014, for a review). Gallet & Bouvier (2013) have shown that the rotational periods of stars as a function of age can be explained if solar-like stars remain magnetically locked to their gaseous inner disks for 5 Myr on average. The rotation rates of the slowest 25% of sources in older clusters (> 10 Myr) requires a longer disk locking time of ~ 7 Myr. There is little evidence that gaseous disks survive that long. Very few young stars are accreting at 5 Myr of age. Using $\text{H}\alpha$ emission as a diagnostic, Fedele et al. (2010) found that 95% of solar-type stars do not show detectable accretion at 5 Myr. The inference of negligible gaseous reservoirs in the inner disk could be avoided if stellar accretion rates are a poor tracer of inner disk gas, i.e., if a substantial fraction of stars with negligible stellar accretion maintain a gas-rich inner disk. However, we find no evidence for residual gas disks surrounding (non-accreting) WTTS. This descriptive result could be made more quantitative when there are theoretical predictions for the amount of residual gas needed for rotational braking to occur.

In contrast, if our observations indicate a gas column density limit of $< 0.17 \text{ g cm}^{-2}$ at 0.5 AU, they are not sensitive enough to determine whether residual gas can whisk away the dust debris generated by terrestrial planet formation and invalidate the commonly held assumption that warm debris disks are tracers of terrestrial planet formation. As discussed by Kenyon et al. (2016), if residual gas is present in the terrestrial planet region at a level $\gtrsim 10^{-5}$ of MMSN, the action of aerodynamic drag and radiation pressure can remove (or prevent the formation of) the debris particles that produce an observable excess.

Measurements that are sensitive to residual gas at this level could weigh in on whether residual gas can resolve a new puzzle: the surprising discrepancy between the high frequency of Earth-mass exoplanets surrounding mature sun-like stars and the lack of evidence for the warm debris that their formation is expected to produce. The occurrence rate of Earth-mass exoplanets at orbital distances of 0.4-1 AU ($\sim 20\%$) is found to be much larger than the incidence rate of warm debris around solar-type stars at ages $\lesssim 10$ Myr (few %). As discussed by Kenyon et al. (2016), a simple way to resolve this discrepancy is if a dilute reservoir of gas (10^{-5} of MMSN) persists for ~ 10 Myr and removes the debris produced by planet formation. More sensitive measures of residual gas than those obtained here, as well as thermal-chemical models tuned to the conditions of dissipating T Tauri disks, are needed to test this hypothesis. Alternative explanations include the possibility that rocky Earth-mass planets are not as common as we think, or that terrestrial planets form very differently than currently imagined, through a process that leaves behind much less debris.

Our results complement stellar accretion rates as a diagnostic of the evolution of gaseous disks. While stellar accretion rates measure the gas mass flux reaching the star, if accretion is halted for some reason, residual gas could remain in the disk despite a low stellar accretion rate. Our results suggest that this outcome is not common: we find that CO ro-vibrational emission is detected only from systems with detectable stellar accretion. However, we cannot rule out the presence of small column densities of residual gas that, while limited in mass, may nevertheless have a significant impact on our ability to detect terrestrial planet formation in action.

Complementary results have been obtained in studies that use alternative *in situ* diagnostics to track the evolution of gaseous disks (see Alexander et al. 2014, for a recent review). Interpreting *Spitzer Space Telescope* upper limits on mid-infrared H_2 line fluxes, Pascucci et al. (2006) inferred gas column density limits $< 10^{-4}$ of MMSN at disk radii > 1 AU in the sample of older stars ($> \text{few Myr}$) studied by FEPS. In contrast to the CO fundamental emission studied here, the FEPS diagnostics are insensitive to, and potentially compromised by, gas close to the star. In the Gorti & Hollenbach (2004) models used to interpret the FEPS upper limits, if the gaseous disk extends in to small radii, the irradiation heating is deposited primarily close to the star and most of the disk is too cool to emit in the *Spitzer* lines. Thus our results complement the FEPS results in probing distances similar to the orbital radii of known exoplanets and the radii where star-disk locking potentially occurs.

UV fluorescent H_2 emission, which is excited by $Ly\alpha$ and arises from similar disk radii as CO fundamental emission, is detected from CTTS, but not WTTS (Ingleby et al. 2009; France et al. 2012). One difficulty with interpreting the lack of fluorescent H_2 emission as evidence for the lack of residual gas is that the fluorescent emission requires both $Ly\alpha$ irradiation and hot H_2 (2000K), neither of which may be abundant in (non-accreting) WTTS.

An alternative UV diagnostic was pursued by Ingleby et al. (2012), who used the 1600\AA feature to infer a short gas dissipation timescale for WTTS disks. The 1600\AA feature is attributed to electron impact excitation of H_2 (Bergin et al. 2004; Ingleby et al. 2009; France et al. 2011).

Because the hot electrons invoked are thought to be produced by X-ray irradiation, and because stellar X-ray irradiation is long-lived (on timescales of tens of Myr), the 1600Å feature is thought to potentially probe residual gas in a non-accreting disk. To confirm this picture, it would be useful to develop models that show that the presence of a residual gas disk would produced a detectable 1600Å feature flux given the typical X-ray luminosity of WTTS.

6. Summary and Conclusions

We have carried out a sensitive search for residual gas and dust in the terrestrial planet region surrounding young stars ranging from a few Myr (Taurus) to ~ 10 Myr (TWA) in age. Using high resolution $4.7\mu\text{m}$ spectra of transition objects and weak T Tauri stars, we searched for weak continuum excesses and CO fundamental emission after making a careful correction for the stellar contribution to the observed spectrum.

We find that the CO emission from transition objects is weaker and located further from the star than CO emission from non-transition T Tauri stars with similar stellar accretion rates. The difference is possibly a chemical effect, i.e., transition objects have robust gaseous disks close to the star, but the CO abundance there is low and weak CO emission results. Alternatively, the gaseous disk close to the star may be truncated by the presence of close-in companions.

Some weak T Tauri stars are found to have weak M -band veiling, but none show CO fundamental emission down to low flux levels ($5 \times 10^{-20} - 10^{-18} \text{ W m}^{-2}$). These limits can potentially lend insights into the ability of residual gas disks to spin down stars, circularize the orbits of terrestrial planets, and whisk away the dusty debris that is expected to serve as a signpost of terrestrial planet formation. To impose these limits, we need to convert our upper limits on CO flux into gas column density upper limits. This conversion requires detailed models of the CO abundance and gas temperature in disk atmospheres with low grain abundance, which are not yet generally available.

If the models of Bruderer (2013), which focus on Herbig stars, are a guide, our limits on CO flux translate into a gas column density of $\lesssim 10^{-4}$ of MMSN at 0.5 AU. Gas disks this tenuous are unlikely to play a major role in circularizing terrestrial planets. At a gas column density of $\sim 10^{-4}$ of MMSN, circularizing terrestrial planets through gas drag requires timescales longer than 10 Myr. The lack of evidence for residual gas in WTTS, as traced by CO also does not help to explain the slow rotation rates of older stars (Bouvier et al. 2014), which require solar-mass stars to remain locked to their disks for ~ 5 Myr (Gallet & Bouvier 2013). This constraint can be made more quantitative when there are theoretical predictions for the amount of residual gas that is needed for rotational breaking to occur.

However, the same upper limit of $\lesssim 10^{-4}$ of MMSN is not sensitive enough to weigh in on whether residual gas whisks away the dusty debris signature of terrestrial planet formation. As described by Kenyon et al. (2016), the unexpected discrepancy between the high frequency of Earth-

mass exoplanets within an AU of mature sun-like stars ($\sim 20\%$) and low incidence rate (few %) of the warm debris that their formation is expected to produce could be explained as a consequence of a long-lived dilute reservoir of residual gas (at a level of $\gtrsim 10^{-5}$ of MMSN) that removes the debris through aerodynamic drag and radiation pressure. This explanation is perhaps more palatable than alternative explanations which include the possibility that rocky Earth-mass planets are not as common as currently estimated or that terrestrial planets form via a much different (neater) process than is currently imagined, producing much less debris.

To pursue these topics more quantitatively, we need to develop thermal-chemical models for T Tauri disks that explore their structure at very low grain abundance. It is also of interest to improve our sensitivity to weak emission from CO and other tracers of gas in the terrestrial planet region. Both higher signal-to-noise spectra and more highly optimized stellar atmosphere corrections would be valuable in this regard.

The authors wish to recognize and acknowledge the very significant cultural role and reverence that the summit of Mauna Kea has always had within the indigenous Hawaiian community. We are most fortunate to have the opportunity to conduct observations from this mountain. We thank the Keck Observatory staff who provided support and assistance during our NIRSPEC run. We thank the anonymous referee for a thorough reading of the manuscript, whose comments helped improve the paper. Financial support for GWD was provided in part by the NASA Origins of Solar Systems program NNH10A0061. JSC acknowledges 6.1 funding for basic research in infrared astronomy at the Naval Research Laboratory. JN acknowledges the stimulating research environment supported by NASA Agreement No. NNX15AD94G to the “Earths in Other Solar Systems” program.

Facility: Keck:II(NIRSPEC).

REFERENCES

- Ádámkovics, M., Glassgold, A. E., & Najita, J. R. 2014, *ApJ*, 786, 135
- Ádámkovics, M., Najita, J. R., & Glassgold, A. E. 2016, *ApJ*, 817, 82
- Agnor, C. B., & Ward, W. R. 2002, *ApJ*, 567, 579
- Alexander, R., Pascucci, I., Andrews, S., Armitage, P., & Cieza, L. 2014, *Protostars and Planets VI*, 475
- Andrews, S. M., Wilner, D. J., Zhu, Z., et al. 2016, *ApJ*, 820, L40
- Andrews, S. M., Rosenfeld, K. A., Kraus, A. L., & Wilner, D. J. 2013, *ApJ*, 771, 129
- Andrews, S. M., Rosenfeld, K. A., Wilner, D. J., & Bremer, M. 2011a, *ApJ*, 742, L5
- Andrews, S. M., Wilner, D. J., Espaillat, C., et al. 2011b, *ApJ*, 732, 42
- Andrews, S. M., & Williams, J. P. 2007, *ApJ*, 671, 1800
- Ardila, D. R., Herczeg, G. J., Gregory, S. G., et al. 2013, *ApJS*, 207, 1
- Balachandran, S., & Carr, J. S. 1994, *Cool Stars, Stellar Systems, and the Sun*, 64, 264
- Banzatti, A., & Pontoppidan, K. M. 2015, *ApJ*, 809, 167
- Baraffe, I., Chabrier, G., Allard, F., & Hauschildt, P. H. 1998, *A&A*, 337, 403
- Baraffe, I., Homeier, D., Allard, F., & Chabrier, G. 2015, *A&A*, 577, A42
- Bergin, E., Calvet, N., Sitko, M. L., et al. 2004, *ApJ*, 614, L133
- Bertout, C., Siess, L., & Cabrit, S. 2007, *A&A*, 473, L21
- Blake, G. A., & Boogert, A. C. A. 2004, *ApJ*, 606, L73
- Bouvier, J., Matt, S. P., Mohanty, S., et al. 2014, *Protostars and Planets VI*, 433
- Briceno, C., Calvet, N., Hernandez, J., et al. 2005, *Star Formation in the Era of Three Great Observatories*, 61
- Brittain, S. D., Rettig, T. W., Simon, T., et al. 2003, *ApJ*, 588, 535
- Brittain, S. D., Simon, T., Najita, J. R., & Rettig, T. W. 2007, *ApJ*, 659, 685
- Brown, J. M., Pontoppidan, K. M., van Dishoeck, E. F., et al. 2013, *ApJ*, 770, 94
- Bruderer, S. 2013, *A&A*, 559, A46

- Cieza, L. A., Schreiber, M. R., Romero, G. A., et al. 2012, *ApJ*, 750, 157
- D’Antona, F. & Mazzitelli, I. 1997, *Mem. Soc. Astron. Italiana*, 68, 823
- de la Reza, R., & Pinzón, G. 2004, *AJ*, 128, 1812
- Dodson-Robinson, S. E., & Salyk, C. 2011, *ApJ*, 738, 131
- Donati, J. F., Moutou, C., Malo, L., et al. 2016, *Nature*, 534, 662
- Eisner, J. A., Hillenbrand, L. A., Carpenter, J. M., & Wolf, S. 2005, *ApJ*, 635, 396
- Espaillet, C., D’Alessio, P., Hernández, J., et al. 2010, *ApJ*, 717, 441
- Espaillet, C., Furlan, E., D’Alessio, P., et al. 2011, *ApJ*, 728, 49
- Espaillet, C., Ingleby, L., Hernández, J., et al. 2012, *ApJ*, 747, 103
- Espaillet, C., Muzerolle, J., Najita, J., et al. 2014, *Protostars and Planets VI*, 497
- Fedele, D., van den Ancker, M. E., Henning, T., Jayawardhana, R., & Oliveira, J. M. 2010, *A&A*, 510, A72
- France, K., Yang, H., & Linsky, J. L. 2011, *ApJ*, 729, 7
- France, K., Schindhelm, E., Herczeg, G. J., et al. 2012, *ApJ*, 756, 171
- Furlan, E., Hartmann, L., Calvet, N., et al. 2006, *ApJS*, 165, 568
- Furlan, E., Forrest, W. J., Sargent, B. A., et al. 2009, *ApJ*, 706, 1194
- Furlan, E., Luhman, K. L., Espaillet, C., et al. 2011, *ApJS*, 195, 3
- Gallet, F., & Bouvier, J. 2013, *A&A*, 556, A36
- Geers, V. C., Pontoppidan, K. M., van Dishoeck, E. F., et al. 2007, *A&A*, 469, L35
- Glassgold, A. E., Meijerink, R., & Najita, J. R. 2009, *ApJ*, 701, 142
- Goorvitch, D. 1994, *ApJS*, 95, 535
- Gorti, U., & Hollenbach, D. 2004, *ApJ*, 613, 424
- Gorti, U., Hollenbach, D., Najita, J., & Pascucci, I. 2011, *ApJ*, 735, 90
- Grankin, K. N. 2013, *Astronomy Letters*, 39, 251
- Hadden, S., & Lithwick, Y. 2014, *ApJ*, 787, 80
- Hartigan, P., Hartmann, L., Kenyon, S., Hewett, R., & Stauffer, J. 1989, *ApJS*, 70, 899

- Hartigan, P., Kenyon, S. J., Hartmann, L., et al. 1991, *ApJ*, 382, 617
- Hauschildt, P. H., Allard, F., & Baron, E. 1999, *ApJ*, 512, 377
- Hernandez, J., Briceno, C., Calvet, N., Hartmann, L., & Muzerolle, J. 2005, *Protostars and Planets V Posters*, 8391
- Herczeg, G. J., & Hillenbrand, L. A. 2014, *ApJ*, 786, 97
- Hillenbrand, L., Slesnick, C., & White, R. 2005, *Spitzer Proposal*, 20103
- Hoadley, K., France, K., Alexander, R. D., McJunkin, M., & Schneider, P. C. 2015, *ApJ*, 812, 41
- Ingleby, L., Calvet, N., Bergin, E., et al. 2009, *ApJ*, 703, L137
- Ingleby, L., Calvet, N., Bergin, E., et al. 2011, *ApJ*, 743, 105
- Ingleby, L., Calvet, N., Herczeg, G., & Briceño, C. 2012, *ApJ*, 752, L20
- Ireland, M. J., & Kraus, A. L. 2008, *ApJ*, 678, L59
- Johns-Krull, C. M., Valenti, J. A., & Saar, S. H. 2004, *ApJ*, 617, 1204
- Kenyon, S. J., & Bromley, B. C. 2004, *ApJ*, 602, L133
- Kenyon, S. J., & Hartmann, L. 1995, *ApJS*, 101, 117
- Kenyon, S. J., Najita, J. R., & Bromley, B. C. 2016, *ApJ*, 831, 8
- Kervella, P., Mérand, A., Pichon, B., et al. 2008, *A&A*, 488, 667
- Kominami, J., & Ida, S. 2002, *Icarus*, 157, 43
- Kominami, J., & Ida, S. 2004, *Icarus*, 167, 231
- Kóspál, Á., Moór, A., Juhász, A., et al. 2013, *ApJ*, 776, 77
- Kraus, A. L., Ireland, M. J., Martinache, F., & Hillenbrand, L. A. 2011, *ApJ*, 731, 8
- Kraus, A. L., & Ireland, M. J. 2012, *ApJ*, 745, 5
- Leinhardt, Z. M., Dobinson, J., Carter, P. J., & Lines, S. 2015, *ApJ*, 806, 23
- Low, F. J., Smith, P. S., Werner, M., et al. 2005, *ApJ*, 631, 1170
- Luck, R. E., & Heiter, U. 2005, *AJ*, 129, 1063
- Luhman, K. L., Allen, P. R., Espaillat, C., Hartmann, L., & Calvet, N. 2010, *ApJS*, 186, 111
- Mahmud, N. I., Crockett, C. J., Johns-Krull, C. M., et al. 2011, *ApJ*, 736, 123

- Mamajek, E. E. 2009, in *EXOPLANETS AND DISKS: THEIR FORMATION AND DIVERSITY: Proceedings of the International Conference*. AIP Conference Proceedings, Volume 1158, pp. 3-10
- Massey, P., Valdes, F., Barnes, J. 1992 *A Users's Guide to Reducing Slit Spectra with IRAF*, National Optical Astronomy Observatory
- Massey, P. 1997 *A User's Guide to CCD reductions with IRAF*, National Optical Astronomy Observatory
- Manara, C. F., Testi, L., Rigliaco, E., et al. 2013, *A&A*, 551, A107
- McLean, I. S., Becklin, E. E., Bendiksen, O., et al. 1998, *Proc. SPIE*, 3354, 566
- Moeckel, N., & Armitage, P. J. 2012, *MNRAS*, 419, 366
- Muzerolle, J., Allen, L. E., Megeath, S. T., Hernández, J., & Gutermuth, R. A. 2010, *ApJ*, 708, 1107
- Natta, A., Testi, L., & Randich, S. 2006, *A&A*, 452, 245
- Najita, J., Carr, J. S., & Mathieu, R. D. 2003, *ApJ*, 589, 931
- Najita, J. R., Carr, J. S., Glassgold, A. E., & Valenti, J. A. 2007, *Protostars and Planets V*, 507
- Najita, J. R., Crockett, N., & Carr, J. S. 2008, *ApJ*, 687, 1168
- Najita, J. R., Carr, J. S., Strom, S. E., et al. 2010, *ApJ*, 712, 274
- Najita, J. R., Andrews, S. M., & Muzerolle, J. 2015, *MNRAS*, 450, 3559
- Neuhäuser, R., Brandner, W., Eckart, A., et al. 2000, *A&A*, 354, L9
- Neuhäuser, R., Potter, D., & Brandner, W. 2001, *arXiv:astro-ph/0106304*
- Nguyen, D. C., Brandeker, A., van Kerkwijk, M. H., & Jayawardhana, R. 2012, *ApJ*, 745, 119
- Padgett, D. L. 1996, *ApJ*, 471, 847
- Pascucci, I., Gorti, U., Hollenbach, D., et al. 2006, *ApJ*, 651, 1177
- Pascucci, I., Hollenbach, D., Najita, J., et al. 2007, *ApJ*, 663, 383
- Pontoppidan, K. M., Blake, G. A., van Dishoeck, E. F., et al. 2008, *ApJ*, 684, 1323-1329
- Raymond, S. N., Armitage, P. J., Moro-Martín, A., et al. 2011, *A&A*, 530, A62
- Raymond, S. N., Armitage, P. J., Moro-Martín, A., et al. 2012, *A&A*, 541, A11
- Rebull, L. M., Padgett, D. L., McCabe, C.-E., et al. 2010, *ApJS*, 186, 259

- Reid, N. 2003, MNRAS, 342, 837
- Rettig, T. W., Haywood, J., Simon, T., Brittain, S. D., & Gibb, E. 2004, ApJ, 616, L163
- Rettig, T., Brittain, S., Simon, T., et al. 2006, ApJ, 646, 342
- Rice, W. K. M., Armitage, P. J., Wood, K., & Lodato, G. 2006, MNRAS, 373, 1619
- Sallum, S., Follette, K. B., Eisner, J. A., et al. 2015, Nature, 527, 342
- Salyk, C., Blake, G. A., Boogert, A. C. A., & Brown, J. M. 2007, ApJ, 655, L105
- Salyk, C., Pontoppidan, K. M., Blake, G. A., et al. 2008, ApJ, 676, L49
- Salyk, C., Blake, G. A., Boogert, A. C. A., & Brown, J. M. 2009, ApJ, 699, 330
- Salyk, C., Pontoppidan, K. M., Blake, G. A., Najita, J. R., & Carr, J. S. 2011, arXiv:1104.0948
Salyk, C., et al. ApJ, submitted 2011
- Salyk, C., Herczeg, G. J., Brown, J. M., et al. 2013, ApJ, 769, 21
- Salyk, C., Lacy, J. H., Richter, M. J., et al. 2015, ApJ, 810, L24
- Santos, N. C., Melo, C., James, D. J., et al. 2008, A&A, 480, 889
- Schaefer, G. H., Simon, M., Beck, T. L., Nelan, E., & Prato, L. 2006, AJ, 132, 2618
- Shabram, M., Demory, B.-O., Cisewski, J., Ford, E. B., & Rogers, L. 2016, ApJ, 820, 93
- Siess, L., Dufour, E., & Forestini, M. 2000, A&A, 358, 593
- Sicilia-Aguilar, A., Hartmann, L., Calvet, N., et al. 2006, ApJ, 638, 897
- Sicilia-Aguilar, A., Henning, T., & Hartmann, L. W. 2010, ApJ, 710, 597
- Simon, M. N., Pascucci, I., Edwards, S., et al. 2016, ApJ, 831, 169
- Snedden, C. 1973 PhD Thesis, University of Texas at Austin
- Tognelli, E., Prada Moroni, P. G., & Degl’Innocenti, S. 2011, A&A, 533, A109
- Torres, G., Guenther, E. W., Marschall, L. A., et al. 2003, AJ, 125, 825
- Vollmann, K. & Eversberg, T. 2006, Astron. Nachr. AN 327, No.9 , 862
- Valenti, J. A., Basri, G., & Johns, C. M. 1993, AJ, 106, 2024
- Van Eylen, V., & Albrecht, S. 2015, ApJ, 808, 126
- Walter, F. M., Brown, A., Mathieu, R. D., Myers, P. C., & Vrba, F. J. 1988, AJ, 96, 297

- Webb, R. A., Zuckerman, B., Platais, I., et al. 1999, *ApJ*, 512, L63
- Weinberger, A. J., Anglada-Escudé, G., & Boss, A. P. 2013, *ApJ*, 762, 118
- White, R. J., & Hillenbrand, L. A. 2004, *ApJ*, 616, 998
- Williams, J. P., & Cieza, L. A. 2011, *ARA&A*, 49, 67
- Wright, J. T., Marcy, G. W., Howard, A. W., et al. 2012, *ApJ*, 753, 160
- Yang, H., Johns-Krull, C. M., & Valenti, J. A. 2008, *AJ*, 136, 2286
- Yang, H., Johns-Krull, C. M., & Valenti, J. A. 2005, *ApJ*, 635, 466
- Zhu, Z., Nelson, R. P., Hartmann, L., Espaillat, C., & Calvet, N. 2011, *ApJ*, 729, 47
- Zhu, Z., Nelson, R. P., Dong, R., Espaillat, C., & Hartmann, L. 2012, *ApJ*, 755, 6

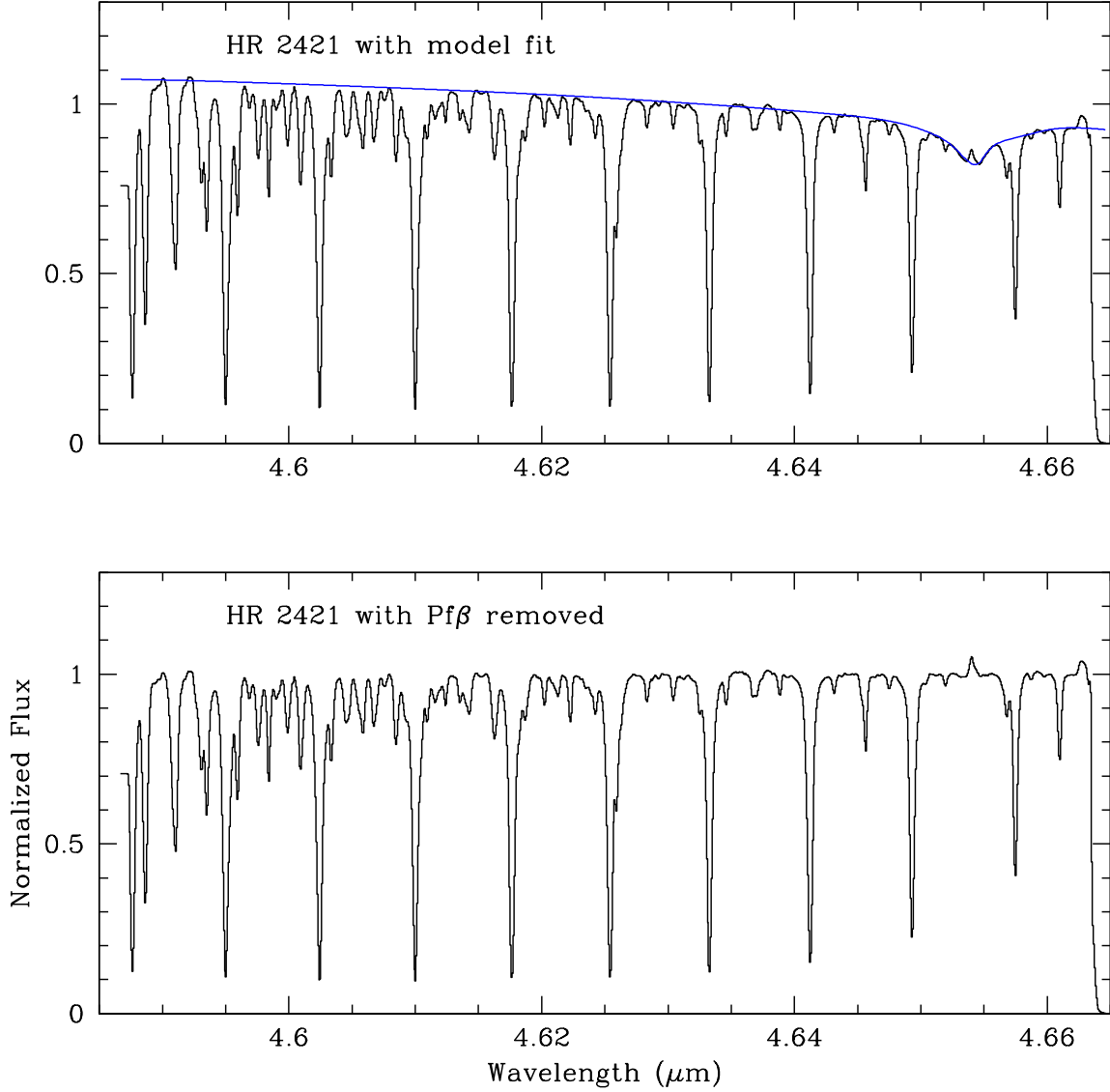


Fig. 1.— The observed spectrum of an early type standard star, HR 2421 (A0 IV) showing broad Pf β absorption (black plot in top panel). A spline is fit to the 4.6 μ m continuum of HR 2421 to model the broad shape of the Pf β absorption line (blue line in top panel). Dividing the observed spectrum by the spline fit removes the broad Pf β emission in the observed telluric spectrum (bottom panel), which is then used to remove the narrow telluric features without altering the shape of the Pf β emission that may be present in our YSO targets.

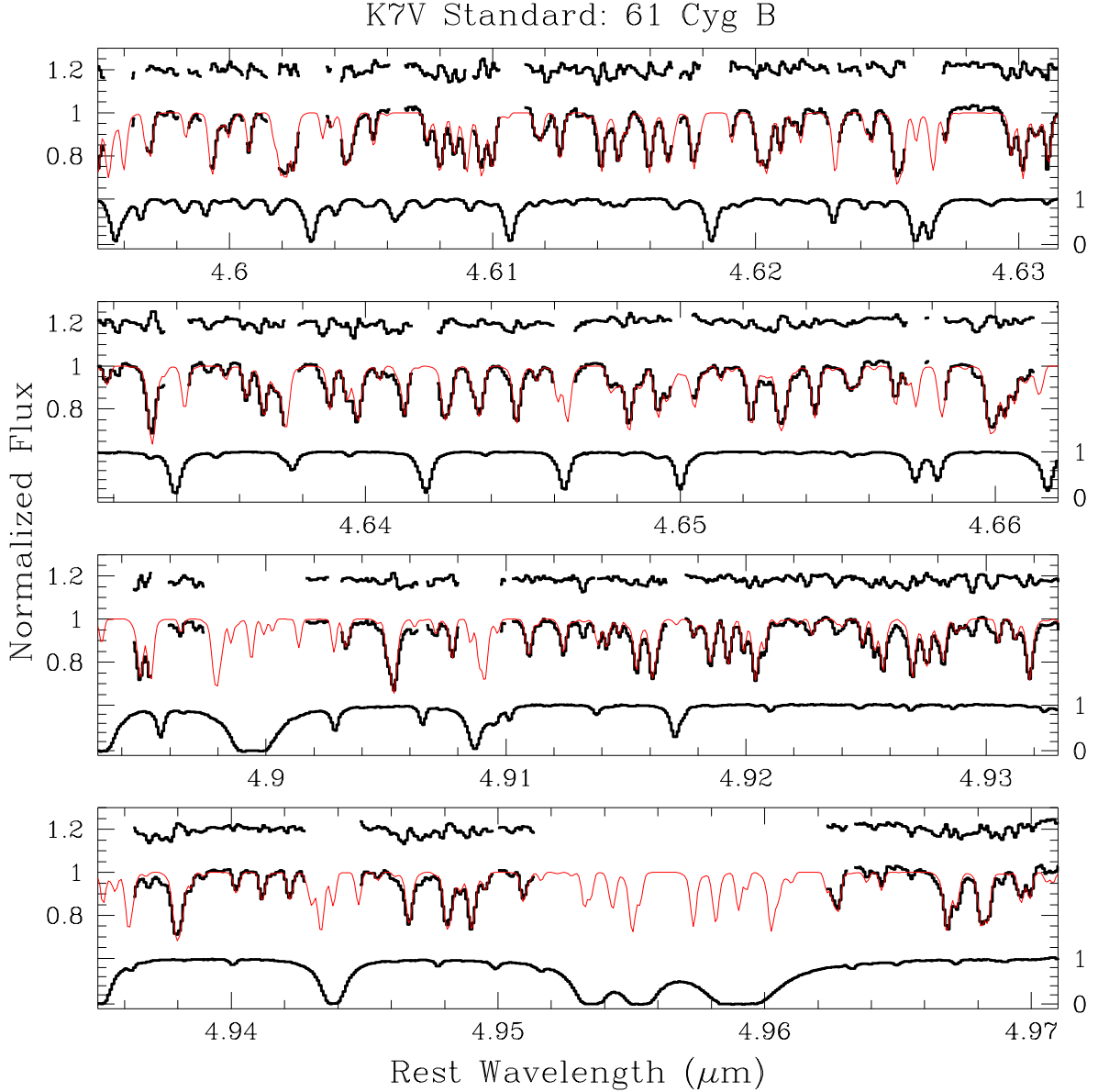


Fig. 2.— Comparison of model fit and observed spectrum of 61 Cyg B, a K7V standard star. In each panel, the observed spectrum (thick black histogram) and model fit (thin red line) are shown, along with the residuals (upper black histogram) and the telluric spectrum (lower black line) for comparison. The observations are well fit by a model with $T_{\text{eff}} = 4000\text{K}$, $\log g = 4.5$ g cm^{-2} , $[\text{Fe}/\text{H}] = -0.27$, and no continuum veiling, consistent with the properties of a late-type main-sequence dwarf. We searched a range of veiling values ($r_{\text{M}} = -0.3$ to 0.4 in steps of 0.1), and found the best fit at zero veiling. Many of the observed residual absorption features not fit by the model in the lower two panels (i.e., $4.91\text{--}4.94\ \mu\text{m}$, $4.945\text{--}4.95\ \mu\text{m}$, and $4.963\text{--}4.97\ \mu\text{m}$) are consistent with water lines identified in the solar sunspot atlas.

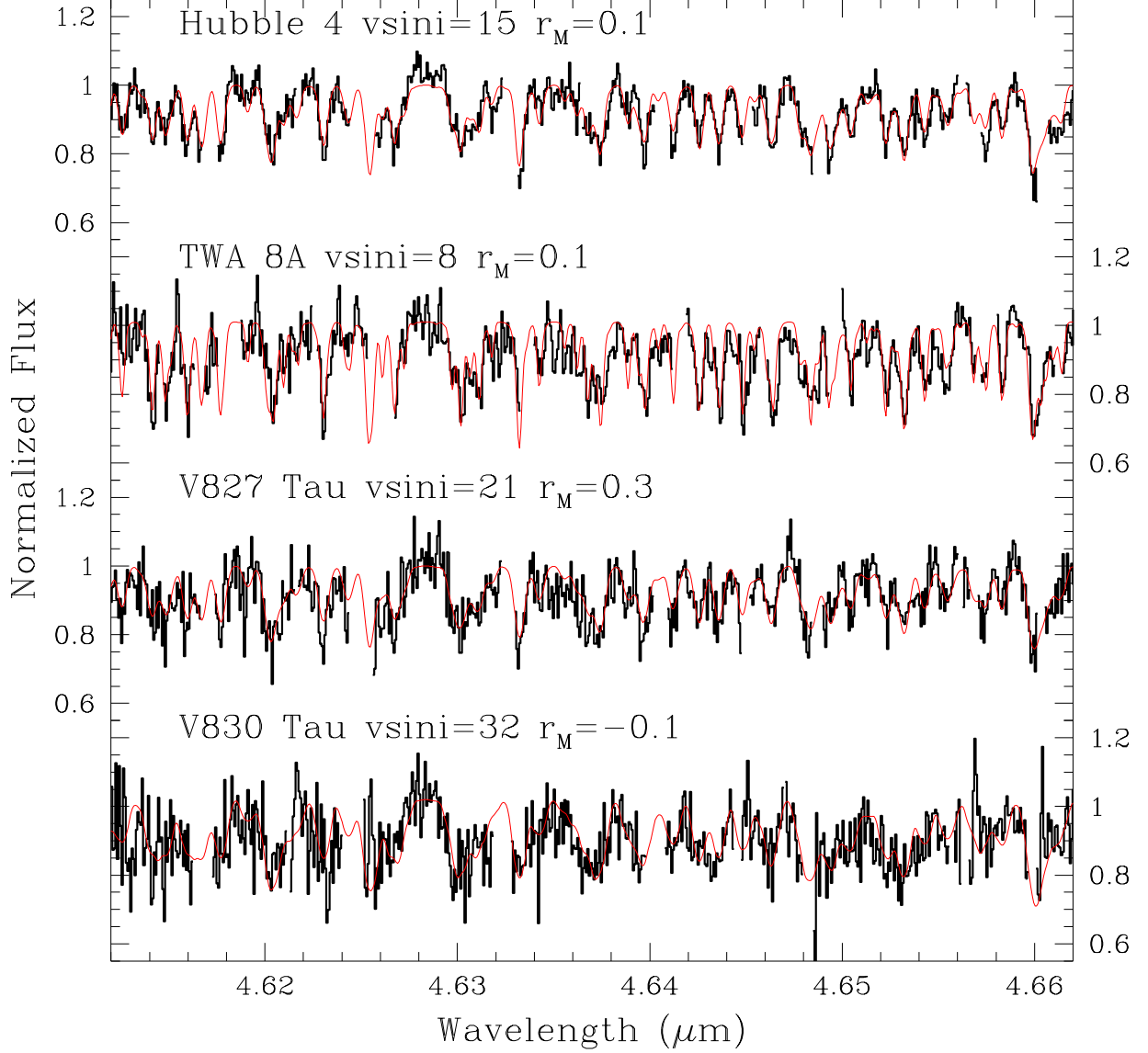


Fig. 3a.— Model fits (thin red lines) to the $4.6\mu\text{m}$ spectra of representative sources (thick black histogram) that have little or no veiling ($r_M \leq 0.3$). The model fits to these WTTS do a reasonable job fitting a range of $v \sin i$ ($8 - 32 \text{ km s}^{-1}$, see Tables 1 and 2) at both $4.6\mu\text{m}$ and $4.9\mu\text{m}$. Spectral regions with poor telluric transmission ($\leq 80\%$) have been excised from the plot.

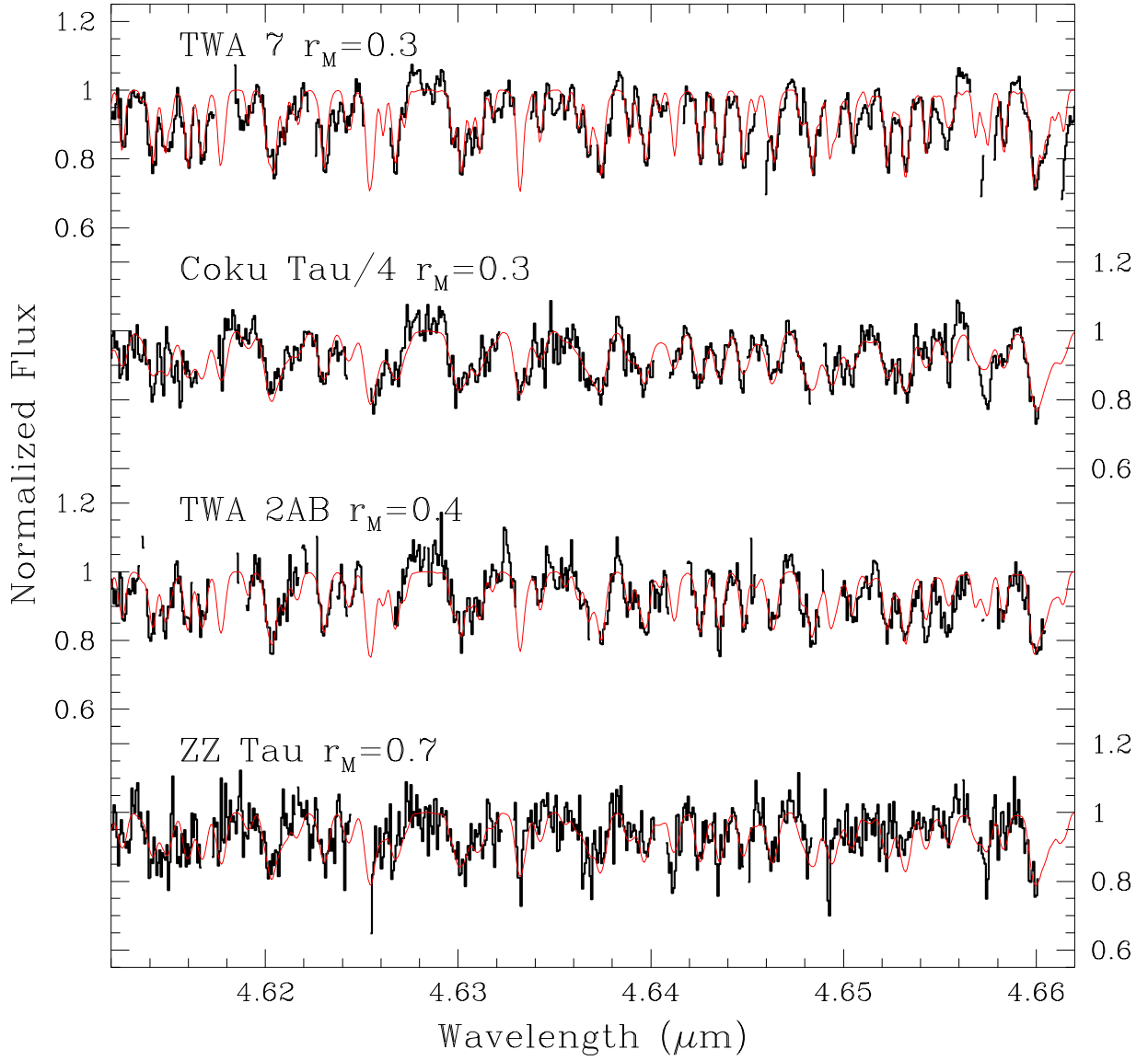


Fig. 3b.— As in Fig. 3a but for sources with veiling r_M from 0.3–0.7, including Coku Tau/4, a transition object, and ZZ Tau, a CTTS.

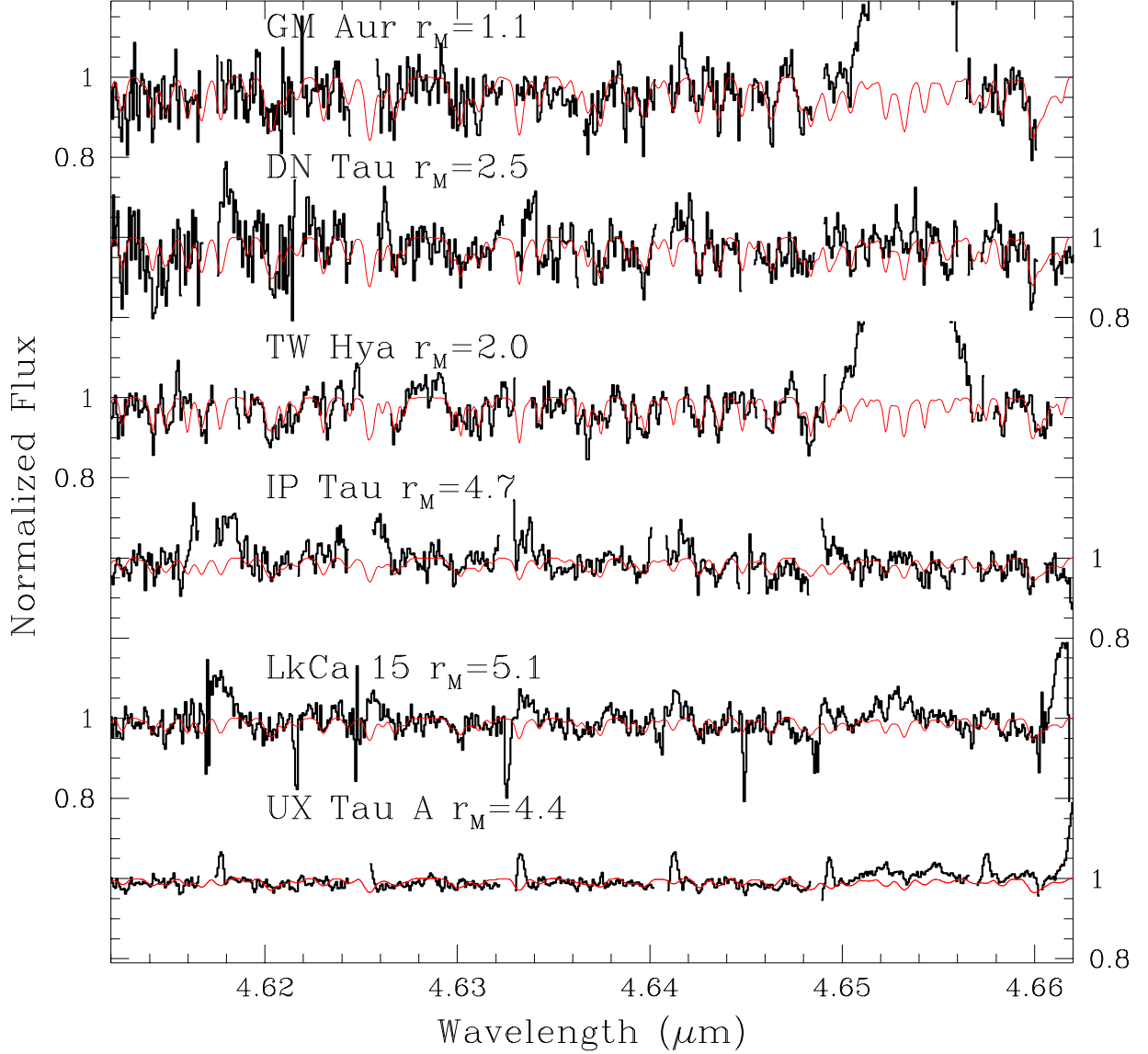


Fig. 3c.— As in Fig 3a but for sources with high veiling ($r_M = 1.1$ – 5.1). Numerous absorption lines in the model fit are coincident with detected emission lines in the observed spectra, underscoring the utility of accurately modeling the stellar component in order to detect weak emission that originates from the warm inner disk. Strong Pf β emission is also seen at $4.652\mu\text{m}$ in the spectra of TW Hya and GM Aur.

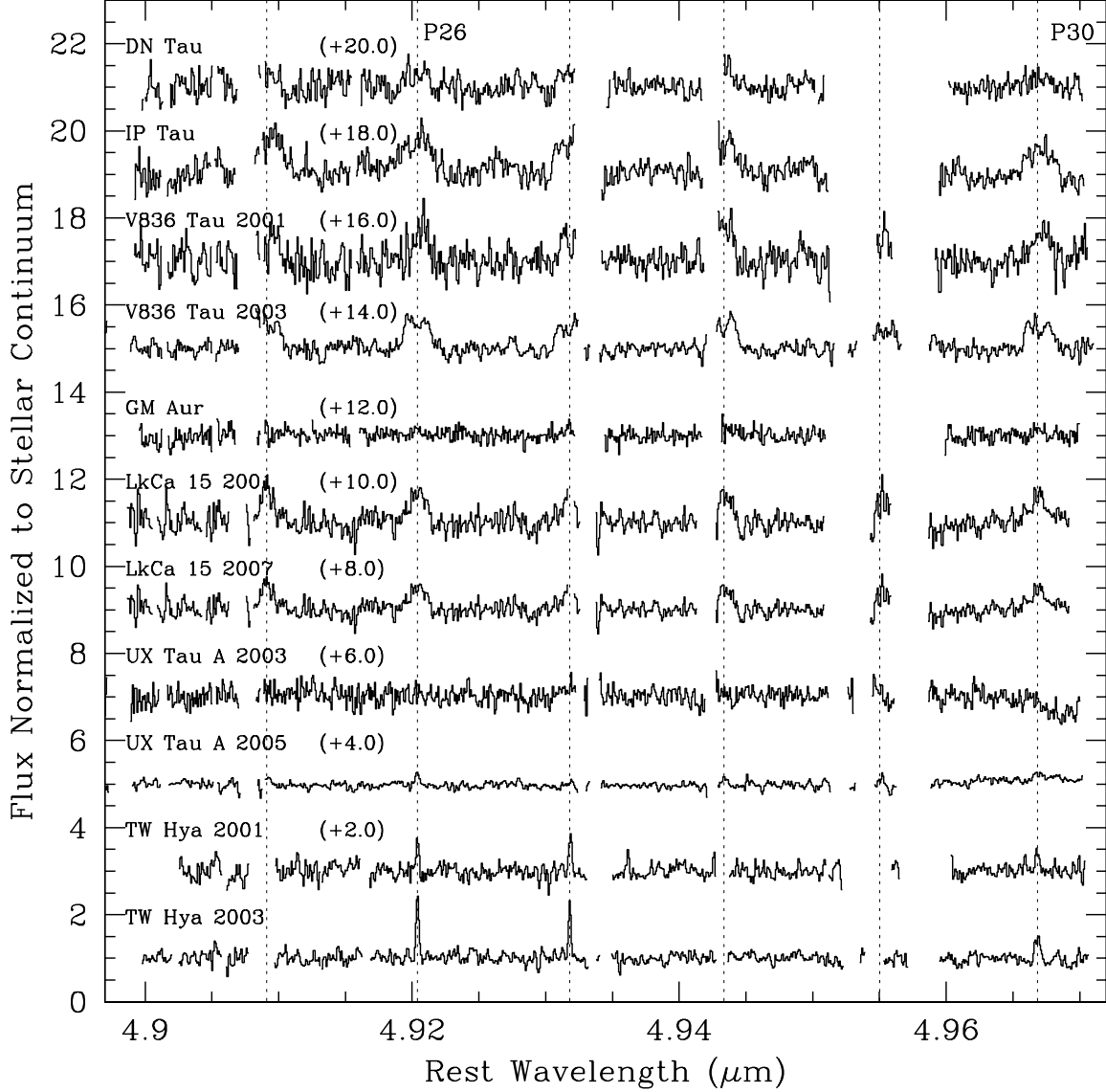


Fig. 4a.— Observed *M*-band spectra with the model veiled stellar photosphere subtracted and replaced with a featureless continuum of equal strength. An arbitrary continuum offset has been added to each spectrum (indicated in parentheses). Only sources with detected high-*J* (P25–P30) CO emission are shown. The residual spectra of CTTS and TOs show CO fundamental emission. The high-*J* lines (P25–P30) shown reveal a range of line strengths and widths. Spectral sub-regions with telluric transmission less than 80% have been excised from the plot.

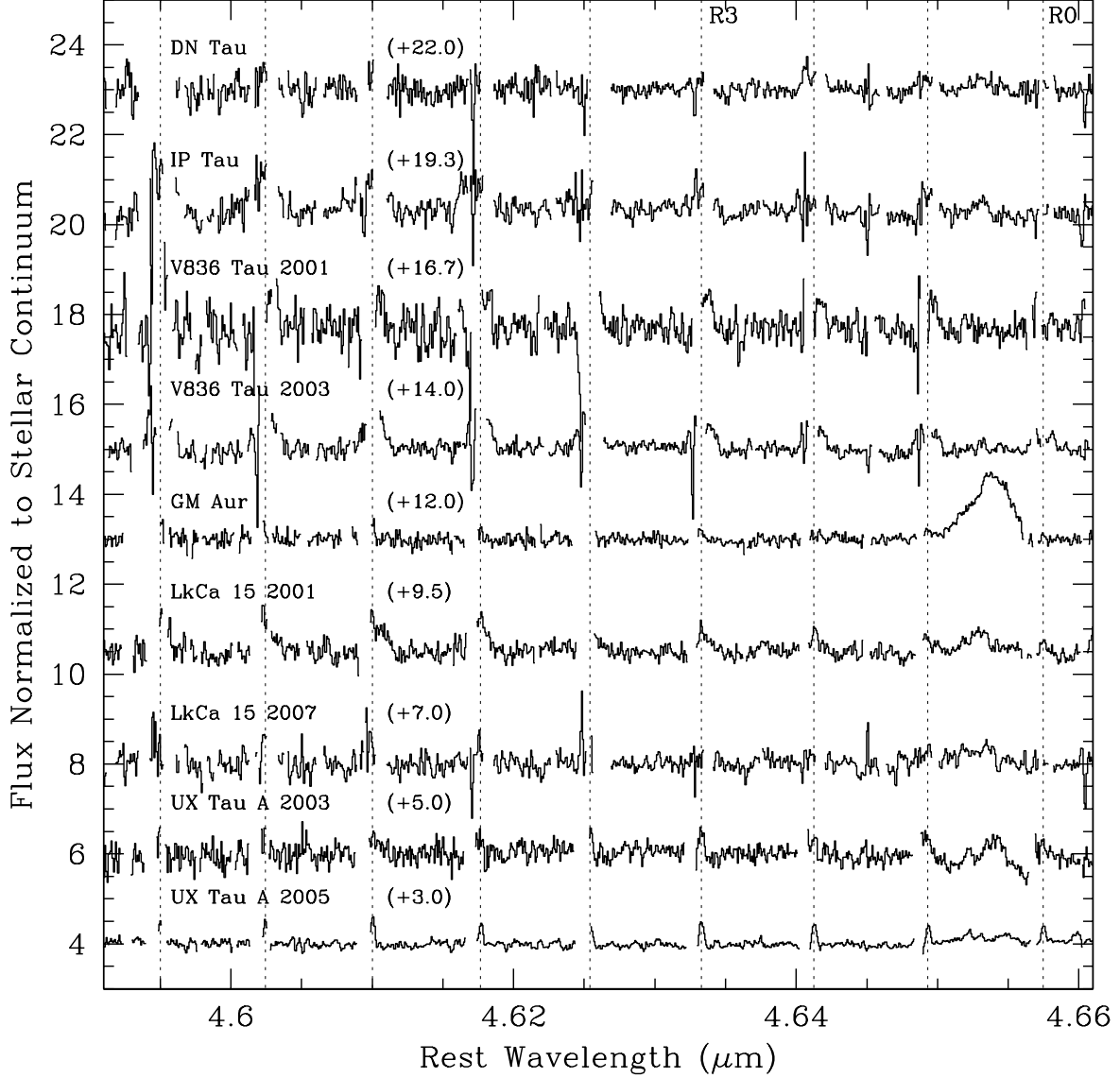


Fig. 4b.— As in Fig. 4a but for low-J lines (R8–R0). $\text{Pf}\beta$ emission is evident in some sources at $4.653\mu\text{m}$. TW Hya, which shows high-J CO emission in our data (Figures 4a and 5), is not included here; the source was not adequately shifted in velocity out of the telluric CO, resulting in poor telluric correction of the low-J CO spectrum.

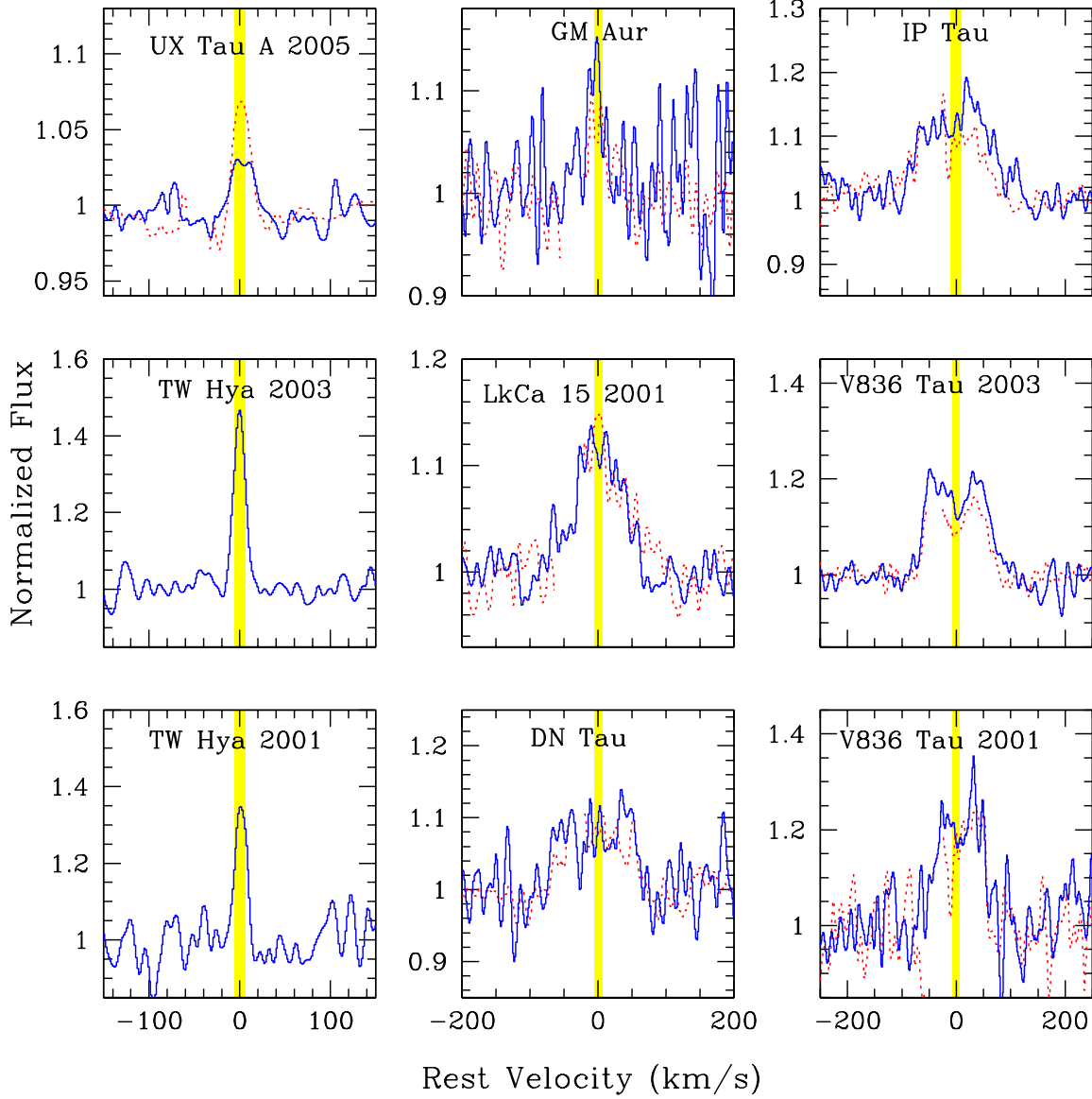


Fig. 5.— CO line profiles, obtained by averaging low-J R-branch lines (dotted red histogram) and high-J P-branch lines (solid blue histogram). FWHM line profiles and equivalent widths are measured from these averaged profiles (see Table 3). The vertical line has the width of a spectral resolution element. Note that the velocity scale differs in each column.

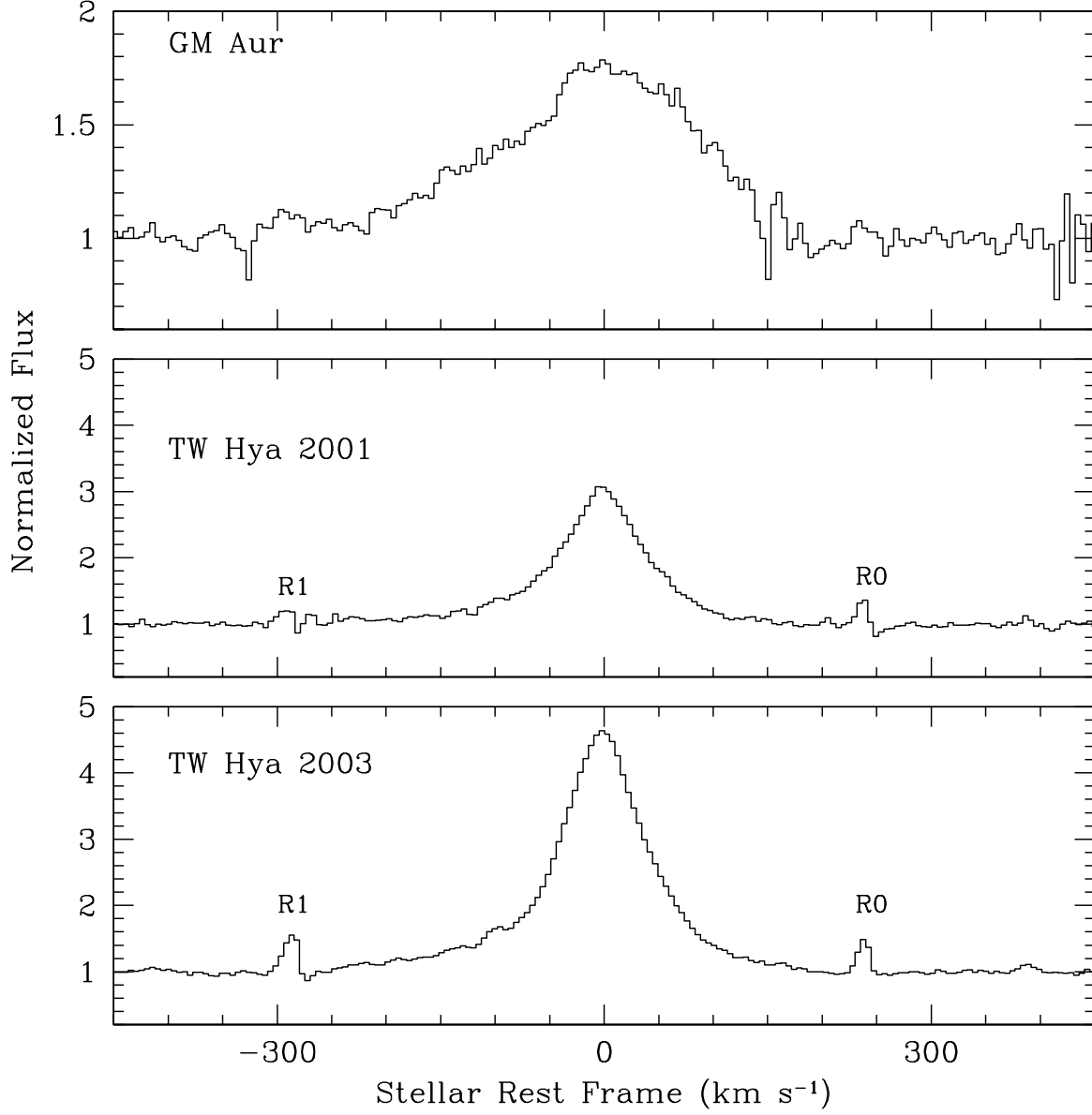


Fig. 6.— Strong Pf β line emission observed in our study. R0 and R1 CO emission lines are indicated in the TW Hya spectrum.

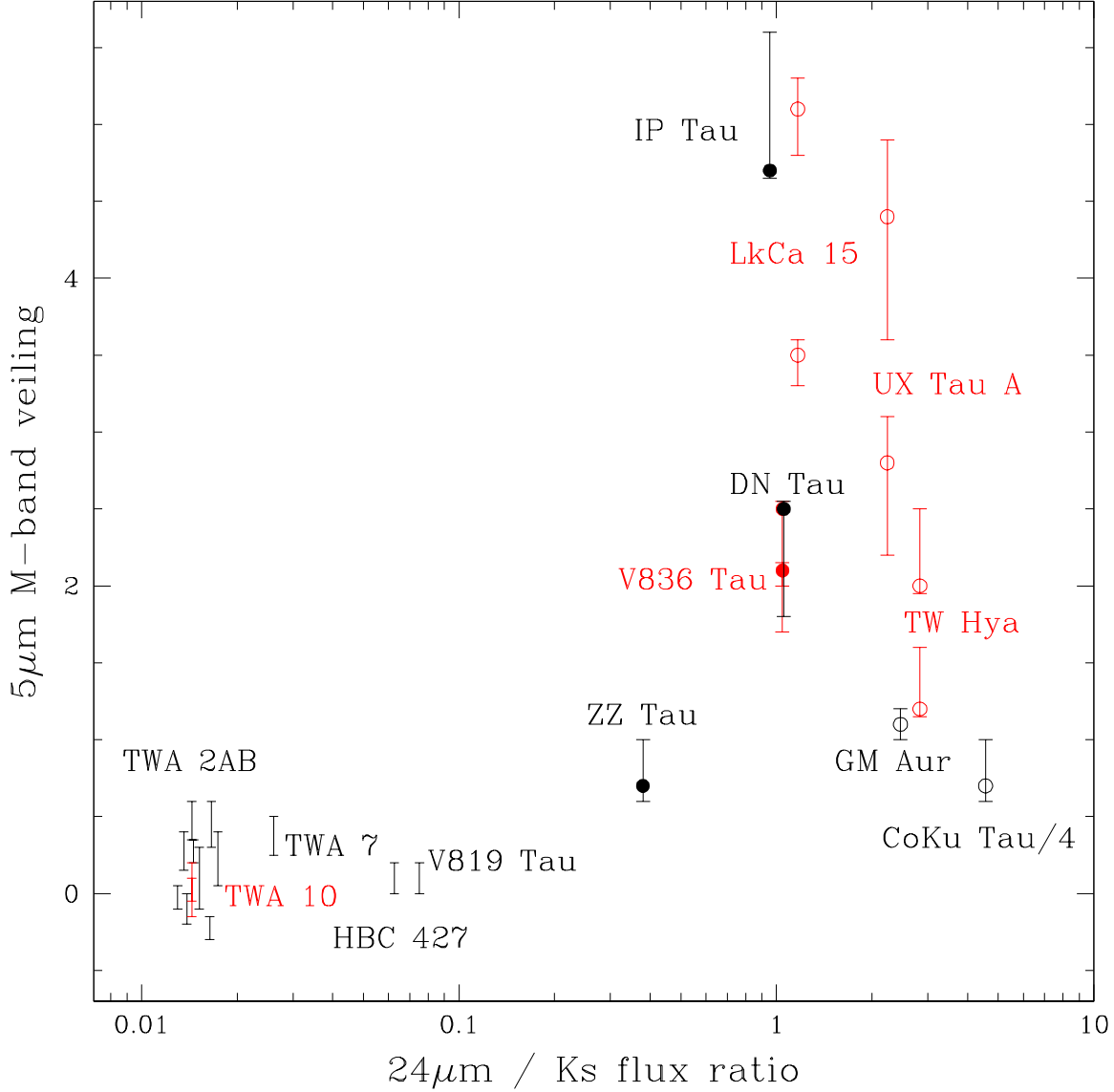


Fig. 7.— Measured M -band veiling vs. mid-infrared color excess. The $24\mu\text{m}$ fluxes (Low et al. 2005; Rebull et al. 2010; Furlan et al. 2006, 2011) have been normalized by the 2MASS K_s flux value. Red points indicate observations made in more than one epoch. Low accretion rate CTTS are shown as solid symbols, while TOs are displayed as open symbols. The tight cluster of objects in the lower left corner are TWA and Taurus WTTS sources in our sample which lack significant M -band veiling. The asymmetric error bars stem from unequal changes in the depths of stellar lines for T_{eff} and $\log g$ pairs that span the uncertainties in those quantities.

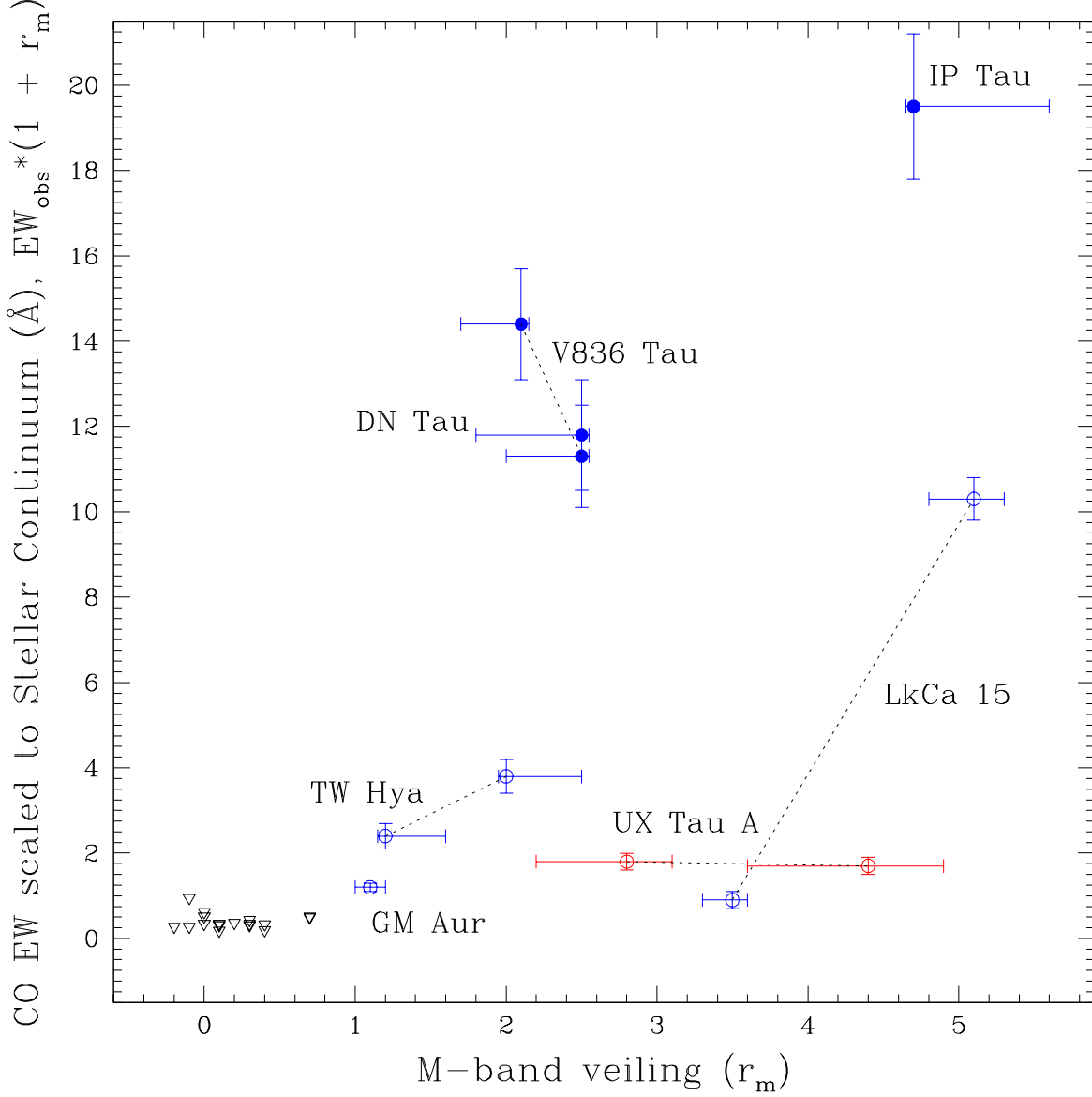


Fig. 8.— Measured M -band veiling vs. CO line flux relative to the stellar continuum for CTTS (filled circles), TOs (open circles), and WTTS (inverted black triangles). CO line strengths are measured from combined R-branch (red) or P-branch (blue) points, respectively. Objects with more than one observational epoch are connected by a dashed line. WTTS, which had no CO emission and little or no veiling, are placed at their 1σ emission detection upper limit for CO equivalent width (lower left corner of plot).

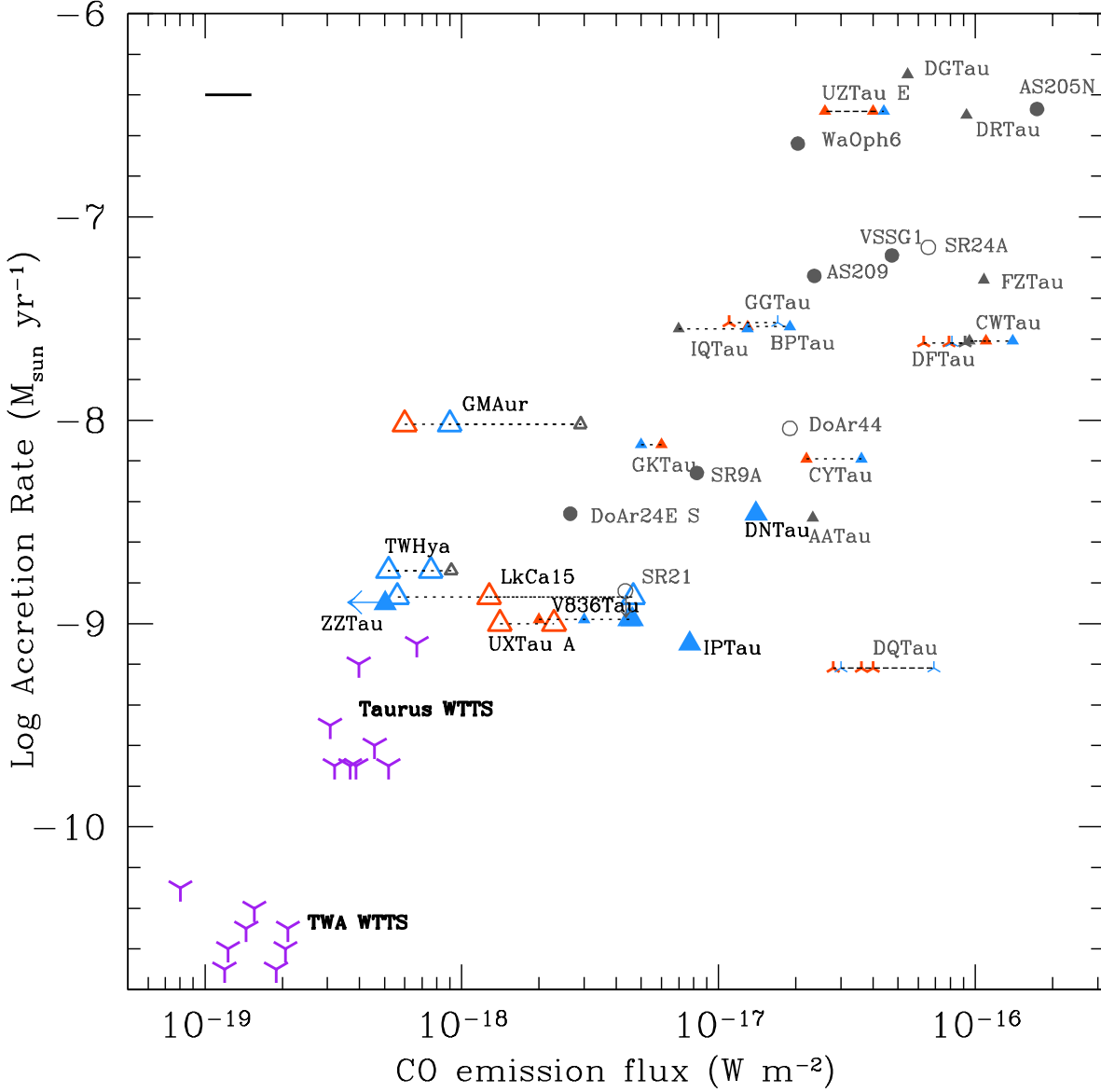


Fig. 9.— CO emission flux vs. stellar accretion rate for TW Hya and sources in Taurus (triangles) and Ophiuchus (circles). Low-J (R0–R5, orange), moderate-J (P8, gray), and high-J lines (P25–P29, blue) are shown for CTTS (solid symbols), TOs (open symbols), and binary sources (skeletal triangles). Objects with multi-epoch observations are connected by a horizontal dotted line. The emission flux for TWA and Ophiuchus sources have been scaled to the same distance as Taurus for comparison. Larger symbol sizes denote objects from this study. A representative 20% error bar in the flux calibration is shown as a horizontal bar. Upper limits for stellar accretion rates and CO line fluxes (an average of the low-J and high-J values) in TWA and Taurus are shown for comparison (inverted purple skeletal triangles). Accretion rate and flux values for targets from other studies are taken from Espaillat et al. (2010); Eisner et al. (2005); Valenti et al. (1993); Natta et al. (2006); Brown et al. (2013); Najita et al. (2007).

Table 1. Journal of Observations and Stellar Parameters

Object	Type ^a	Obs Date (UT)	Int. Time (min.)	SNR 4.630 μ m	Slit Width (arcsec)	SpT	T_{eff} (K)	Ref	$\log g$ (g cm ⁻²)	Ref	$v \sin i$ (km s ⁻¹)	Ref
DN Tau	C	2007 Jan 2+3	64	22	0.43	M0.3	3846	1	3.6	1	12	10
IP Tau	C	2003 Jan 13	48	35	0.72	M0.6	3792	1	3.9	1	12	10
V836 Tau	C	2001 Jan 20	16	17	0.43	M0.8	3756	1	4.0	1	13	10
V836 Tau	C	2003 Jan 11	40	30	0.43	M0.8	3756	1	4.0	1	13	10
ZZ Tau	C	2001 Jan 20	12	20	0.43	M4.3	3127	1	3.0	1	22	11
CoKu Tau/4	W,T	2005 Feb 18+19	190	30	0.58	M1.1	3704	1	3.9	1	26	10
GM Aur	C,T	2001 Jan 19	16	25	0.43	K6.0	4115	1	4.1	1	15	10
LkCa 15	C,T	2001 Jan 19	16	50	0.43	K5.5	4163	1	3.9	1	14	10
LkCa 15	C,T	2007 Jan 2+3	84	40	0.43	K5.5	4163	1	3.9	1	14	10
UX Tau A	C,T	2003 Jan 11	48	30	0.43	K0	5250 ^b	2	4.5 ^b	2	24	10
UX Tau A	C,T	2005 Feb 19	56	90	0.43	K0	5250 ^b	2	4.5 ^b	2	24	10
HBC 427	W	2003 Jan 13	16	15	0.58	K6.0	4115	1	3.8	1	10	10
Hubble 4	W	2003 Jan 13	24	25	0.58	K7	4158 ^b	3	3.6 ^b	3	15	3
IW Tau	W	2003 Jan 12	44	15	0.72	M0.9	3738	1	3.7	1	9	10
LkCa 19	W	2003 Jan 12	48	15	0.43	K0	5100 ^b	2	3.8 ^b	2	20	10
V410 Tau	W	2001 Jan 20	6	16	0.43	K3	4730	4	4.1	7,9	83	10
V819 Tau	W	2003 Jan 12	48	15	0.43	K8.0	3980	1	4.0	1	9	10
V827 Tau	W	2003 Jan 13	36	20	0.58	M1.4	3656	1	3.8	1	21	10
V830 Tau	W	2003 Jan 12	48	12	0.43	K7.5	4000	1	3.9	1	32	10
TW Hya	C,T	2001 Jan 20	12	25	0.43	K7	4126 ^b	5	4.8 ^b	5	6	5
TW Hya	C,T	2003 Jan 11	40	30	0.43	K7	4126 ^b	5	4.8 ^b	5	6	5
TWA 2AB	W	2003 Jan 13	40	30	0.58	M2.2	3530	1	3.9	1	13	12
TWA 5	W	2003 Jan 12	26	55	0.58	M2.7	3455	1	3.7	1	55 ^c	12
TWA 6	W	2003 Jan 12	32	18	0.58	M0.0	3900	1	4.3	1	55	13
TWA 7	W	2003 Jan 12	32	50	0.58	M3.2	3366	1	3.9	1	2	13
TWA 8A	W	2001 Jan 20	16	25	0.43	M2.9	3425	1	4.0	1	8 ^d	13
TWA 9A	W	2003 Jan 13	28	10	0.58	K6.0	4115	1	4.5	1	9	14
TWA 10	W	2001 Jan 20	8	7	0.43	M2.5	3525	6	4.3	8,9	2	8
TWA 10	W	2003 Jan 11	44	12	0.43	M2.5	3525	6	4.3	8,9	2	8

^aAccreting sources (CTTS) with a transition object SED are designated ‘C,T’. All other CTTS are designated ‘C’. Non-accreting sources (WTTS) with a transition object SED are designated ‘W,T’. All other WTTS are designated ‘W’.

^b T_{eff} and $\log g$ reported directly from spectroscopic measurements

^cA better model fit was found using 55 instead of 36 km s⁻¹ from the literature

^dA better model fit was found using 8 instead of < 3 km s⁻¹ from the literature

Note. — (1) Herczeg & Hillenbrand (2014), (2) Balachandran & Carr (1994), (3) Johns-Krull et al. (2004), (4) Kenyon & Hartmann (1995), (5) Yang et al. (2005), (6) Webb et al. (1999), (7) Bertout et al. (2007), (8) de la Reza & Pinzón (2004), (9) Baraffe et al. (2015), (10) Nguyen et al. (2012), (11) White & Hillenbrand 2004, (12) Torres et al. (2003), (13) Reid (2003), (14) Yang et al. (2008)

Table 2. Model Parameters and Derived Properties

Object	$T_{\text{eff}}^{\text{a}}$ (K)	$\log g^{\text{a}}$ (g cm^{-2})	Veiling (r_{M})	Radial Velocity ^b v_{helio} (km s^{-1})
DN Tau	3800	3.5	2.5 (+0.05, −0.7)	16
IP Tau	3800	4.0	4.7 (+0.9, −0.05)	16
V836 Tau (2001)	3800	4.0	2.1 (+0.05, −0.4)	18
V836 Tau (2003)	3800	4.0	2.5 (+0.05, −0.5)	18
ZZ Tau	3400	3.5	0.7 (+0.3, −0.1)	18
CoKu Tau/4	3700	4.0	0.3 (+0.2, −0.05)	16
GM Aur	4200	4.0	1.1 ± 0.1	15
LkCa 15 (2001)	4200	4.0	5.1 (+0.2, −0.3)	18
LkCa 15 (2007)	4200	4.0	3.5 (+0.1, −0.2)	18
UX Tau A (2003)	5200	4.5	2.8 (+0.3, −0.6)	16
UX Tau A (2005)	5200	4.5	4.4 (+0.5, −0.8)	16
HBC 427	4200	4.0	0.1 ± 0.1	17
Hubble 4	4200	3.5	0.1 (+0.3, −0.05)	14
IW Tau	3700	3.5	0.3 (+0.05, −0.1)	16
LkCa 19	5000	4.0	0.0 (+0.05, −0.1)	13
V410 Tau	4800	4.0	−0.2 (+0.05, −0.1)	20
V819 Tau	4000	4.0	0.1 ± 0.1	17
V827 Tau	3700	4.0	0.3 (+0.3, −0.05)	18
V830 Tau	4000	4.0	−0.1 ± 0.1	18
TW Hya (2001)	4200	4.5	1.2 (+0.4, −0.05)	13
TW Hya (2003)	4200	4.5	2.0 (+0.5, −0.05)	13
TWA 2AB	3500	4.0	0.4 (+0.2, −0.05)	11
TWA 5	3500	3.5	0.4 (+0.2, −0.1)	15
TWA 6	3900	4.5	0.2 (+0.2, −0.05)	17
TWA 7	3400	4.0	0.3 (+0.2, −0.05)	12
TWA 8A	3400	4.0	0.1 ± 0.2	8
TWA 9A	4200	4.5	0.0 (+0.05, −0.1)	10
TWA 10 (2001)	3500	4.5	−0.1 (+0.2, −0.05)	7
TWA 10 (2003)	3500	4.5	0.0 (+0.2, −0.05)	7

^aUsed stellar atmosphere model that was closest to literature values reported in Table 1

^bMeasured radial velocities are in agreement with literature values except for the following spectroscopic binaries: HBC 427, Hubble 4, and TWA 5

Table 3. Measured CO Emission Properties

Object	CO (1-0) low J				CO (1-0) high J			
	EW ^b (Å)	error ^b	FWHM (km s ⁻¹)	J lines used	EW ^b (Å)	error ^b	FWHM (km s ⁻¹)	J lines used
DN Tau ^a	2.26	±0.03	128	R1-3	3.37	±0.07	130	P26,P30
IP Tau ^a	2.18	±0.04	108	R3-5	3.42	±0.05	120-150	P25-P28
V836 Tau (2001) ^a	3.88	±0.12	125	R2,R3,R5	4.65	±0.24	85	P27,P28,P30
V836 Tau (2003) ^a	3.19	±0.05	128	R1,R3,R5	3.24	±0.20	120	P26,P28,P30
ZZ Tau	< 0.30	-	-	R3	< 0.35	-	-	P26
CoKu Tau/4	< 0.29	-	-	R3	< 0.34	-	-	P26
GM Aur	0.33	±0.01	22	R2,R3,R5	0.56	±0.01	30	P26-27
LkCa 15 (2001)	0.34	±0.01	~20	R2,R3,R5	1.68	±0.04	73	P25-28
LkCa 15 (2007)	< 0.29	-	-	R3	0.2	±0.05	30	P26-27,P30
UX Tau A (2003)	0.48	±0.03	30	R0-3	< 0.24	-	-	P26
UX Tau A (2005)	0.31	±0.01	22	R0-3	0.19	±0.01	28	P25-26,P28-29
HBC 427	< 0.31	-	-	R3	< 0.33	-	-	P26
Hubble 4	< 0.16	-	-	R3	< 0.18	-	-	P26
IW Tau	< 0.34	-	-	R3	< 0.28	-	-	P26
LkCa 19	< 0.34	-	-	R3	< 0.29	-	-	P26
V410 Tau	< 0.34	-	-	R3	< 0.33	-	-	P26
V819 Tau	< 0.28	-	-	R3	< 0.28	-	-	P26
V827 Tau	< 0.24	-	-	R3	< 0.26	-	-	P26
V830 Tau	< 0.31	-	-	R3	< 0.36	-	-	P26
TW Hya (2001)	< 0.36	-	-	R3	1.10	±0.03	16	P26-27
TW Hya (2003)	< 0.43	-	-	R3	1.28	±0.05	15	P26-27
TWA 2AB	< 0.23	-	-	R3	< 0.24	-	-	P26
TWA 5	< 0.13	-	-	R3	< 0.16	-	-	P26
TWA 6	< 0.40	-	-	R3	< 0.34	-	-	P26
TWA 7	< 0.31	-	-	R3	< 0.30	-	-	P26
TWA 8A	< 0.31	-	-	R3	< 0.32	-	-	P26
TWA 9A	< 0.51	-	-	R3	< 0.38	-	-	P26
TWA 10 (2001)	< 1.06	-	-	R3	< 0.53	-	-	P26
TWA 10 (2003)	< 0.62	-	-	R3	< 0.39	-	-	P26

^aAveraged low J lines measured from half width of emission profiles and assuming symmetry

^bEquivalent widths and errors are measured relative to the observed continuum level